



8-2000

Modeling of convective heat transfer coefficient of graphite foam and effective young's modulus of short fiber-reinforced composite

Hairong Li

Follow this and additional works at: https://trace.tennessee.edu/utk_gradthes

Recommended Citation

Li, Hairong, "Modeling of convective heat transfer coefficient of graphite foam and effective young's modulus of short fiber-reinforced composite. " Master's Thesis, University of Tennessee, 2000.
https://trace.tennessee.edu/utk_gradthes/9417

This Thesis is brought to you for free and open access by the Graduate School at TRACE: Tennessee Research and Creative Exchange. It has been accepted for inclusion in Masters Theses by an authorized administrator of TRACE: Tennessee Research and Creative Exchange. For more information, please contact trace@utk.edu.

To the Graduate Council:

I am submitting herewith a thesis written by Hairong Li entitled "Modeling of convective heat transfer coefficient of graphite foam and effective young's modulus of short fiber-reinforced composite." I have examined the final electronic copy of this thesis for form and content and recommend that it be accepted in partial fulfillment of the requirements for the degree of Master of Science, with a major in Mechanical Engineering.

N Yu, Major Professor

We have read this thesis and recommend its acceptance:

Grzegorz Kawiecki, Christopher D. Pionke

Accepted for the Council:

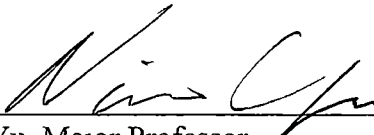
Carolyn R. Hodges

Vice Provost and Dean of the Graduate School

(Original signatures are on file with official student records.)


To the Graduate Council

I am submitting herewith a thesis written by Hairong Li entitled "Modeling of Convective Heat Transfer Coefficient of Graphite Foam and Effective Young's Modulus of Short Fiber-Reinforced Composite" I have examined the final copy of this thesis for form and content and recommend that it be accepted in partial fulfillment of the requirements for the degree of Master of Science, with a major in Mechanical Engineering




N Yu, Major Professor

We have read this thesis
and recommend its acceptance




Grzegorz Kawiecki



Christopher D Pionke

Accepted for the Council



Associate Vice Chancellor
and Dean of The Graduate School

**Modeling of Convective Heat Transfer Coefficient of
Graphite Foam and Effective Young's Modulus of
Short Fiber-Reinforced Composite**

A Thesis

Presented for the

Master of Science Degree

The University of Tennessee, Knoxville

Hairong Li

August, 2000

DEDICATION

This thesis is dedicated to my parents,

HuanGang Li and HeFen Tang

my lovely daughter

XinLan Hu

and especially my soul mate,

Haitian Hu

for all their support and encouragement

ACKNOWLEDGMENT

The author would like to take this opportunity to express her sincere gratitude to Dr. N Allen Yu for his insightful guidance, constant support, and invaluable help. If it were not for Dr Yu's advice, encouragement, and belief in her, so much progress in study and research would not have been possible. The author also wishes to thank Dr Grzegorz Kawiecki and Dr. Christopher D. Pionke for serving on the author's advisory committee, and Dr James Klett and Mr. David P Stinton at Oak Ridge National Laboratory for their support.

The author also wants to thank Mr. Chin C. Tee for his warmhearted help

The author would also like to extend her sincere gratitude to her father, HuanGang Li, her mother, HeFen Tang; and her daughter, XinLan Hu for their love and encouragement. Finally but not the least, the author wants to express her appreciation to her husband, Haitian Hu, for all his love, contribution and support through the years toward her studies and especially toward the completion of this thesis.

The work is supported in part by the Lockheed Martin Energy Research Corporation under Contract No LMER 11X-TA169 to the University of Tennessee (Parent contract sponsored by the U.S. Department of Energy, Assistant Secretary for Energy Efficiency and Renewable Energy, Office of Transportation Technologies, as part of the Advanced Automotive Materials Program, under contract DE-AC-05-96OR22464 with Lockheed Martin Energy Research Corporation), and in part by

National Science Foundation Combined Research Curriculum Development Program
under Grant No. NSF-EEC-9527527.

ABSTRACT

The present work can be divided into two parts: (1) the analytical modeling on the overall convective heat transfer coefficient of porous graphite foam, developed at the Oak Ridge National Laboratory, and (2) the finite element analysis on effective Young's modulus of short fiber-reinforced composite. The present efforts focus on the relationship between the vital microstructural parameters (e.g., pore size, porosity, fiber aspect ratio, etc.) and overall properties (e.g., convective heat transfer coefficient and effective Young modulus) of novel graphite foams and discontinuous fiber-reinforced composites

The graphite foam developed at the Oak Ridge National Laboratory is a promising candidate for the core material in heat exchangers. To develop graphite foams that exhibit high thermal conductivities, high convective heat transfer coefficients, and acceptable pressure drop across the foam, one must have a clear delineation of the interaction between overall properties and foam microstructure, which in turn, is related to the processing of foam. To this end, an analytical model is developed to explicitly include vital microstructural parameters such as foam porosity and pore size, and properties and free stream velocities of cooling fluids, and to predict the overall convective heat transfer coefficient as well as pressure drop of the graphite foam. The predictions agree well with experimental results.

Not a lot of analytical models are available for estimating the effective properties and the stress transfer in *short* fiber-reinforced or whisker composites. The most popular

ones are shear-lag based models. The validity of the predicted effective Young moduli of short fiber-reinforced composites obtained by the modified shear-lag model is verified by the present finite element analysis. In particular, the effects of fiber volume fraction and fiber aspect ratio on the effective Young modulus of short fiber-reinforced composite are examined. It is concluded that the modified shear-lag model generally provides very accurate estimates on effective longitudinal Young's moduli of short fiber-reinforced composites.

TABLE OF CONTENTS

Chapter	Page
1. Introduction on Graphite Foam	1
1.1 Background... ..	1
1.1.1 Graphite foam.	1
1.1.2 Convective heat transfer.	7
1.1.3 Heat transfer coefficients.....	11
1.2 Literature Review	11
1.3 Nature of the Problem.. .	17
2. Analytical Modeling On Overall Convective Heat Transfer Coefficient of Graphite Foam....	19
2.1 Cubic Cell Model	19
2.1.1 Geometrical representation.....	19
2.1.2 A single cylinder in a cross flow. .	25
2.1.3 A bank of type Z cylinders in cross flow	28
2.1.4 Foam with open cubic cells.....	30
2.1.5 Results	34
2.2 Tetraikadecaeron Cell Model.....	34
2.2.1 The unit cell	34
2.2.2 Fluid velocity profile....	43
2.2.3 Fluid temperature profile... .	46
2.2.4 Pressure drop.....	47
2.2.5 Overall convective heat transfer coefficient.....	52
2.2.6 Results and discussion.....	55
3. Conclusions and Discussion on Graphite Foam.....	68
4. Introduction on Fiber-Reinforced Components.....	72
4.1 Background....	72

4.1.1 Composite materials...	72
4.1.2 Short fiber-reinforced composites.....	73
4.1.3 Unidirectional fibrous composites ...	74
4.2 Literature Review	75
4.3 Scope of Study	78
5. FEA on Effective Young's Modulus of Short Fiber-Reinforced Composite.....	80
5.1 Geometric and material models.	80
5.2 Governing equations and boundary conditions.....	83
5.3 Finite element model.....	85
5.4 Results and discussion.....	88
6. Conclusions and Discussions	101
References	103
Vita	113

LIST OF TABLES

Table 1.1: Properties of graphite foams produced from different precursors (Klett <i>et al</i> , 1999a)	2
Table 1 2: Thermal properties of mesophase pitch-based graphite foams compared with those of traditional thermal management materials (Klett <i>et al</i> , 2000a)	3
Table 2 1. Dimensions and densities of the graphite foam blocks tested in the heat exchanger chamber (Tee, 2000).....	57
Table 5.1 Constituent properties of Al/SiC composite (Hsueh, 2000)....	90
Table 5 2: Properties of SiC particulate- or whisker-reinforced aluminum matrix composites (Hsueh, 2000).. .	92

LIST OF FIGURES

Figure 1.1	Typical microstructure of mesophase pitch-derived graphite foam (Klett, 1999b).....	5
Figure 1.2	Reticulated glassy graphite foam produced by ERG Corporation (Klett, 1999b).....	6
Figure 2.1	Forced convection in porous graphite foam ...	20
Figure 2.2:	Modified domain of forced convection in porous graphite foam	21
Figure 2 3:	Cubic unit cell consisting of struts with a circular cross-sectional area (Lu <i>et al</i> , 1998).	22
Figure 2.4:	Boundary layer formation and separation on a circular cylinder in a cross flow (a)longitudinal view, (b)cross-sectional view (Incropera and DeWitt, 1990).....	26
Figure 2.5.	Overall convective heat transfer coefficient of graphite foam with porosity of 80% as a function of mean cell size, a , for air (20°C) with different velocities.	35
Figure 2 6:	Overall convective heat transfer coefficient of graphite foam with porosity of 80% and different cell sizes as a function of free stream velocity u_{avg} for air (20°C)	36
Figure 2.7:	Stacked tetrakaidecahedron cells: (a) Three-dimensional view (Gibson and Ashby, 1997); (b) Two-dimensional views ...	38
Figure 2.8:	Tetrakaidecahedron unit cell	40
Figure 2.9.	Two-dimensional projection of the mid-plane of the unit cell	40
Figure 2 10	Pressure drop per unit length, $\Delta p/L_p$, across graphite foam ($D = 300\mu\text{m}$; $\phi = 80\%$) as a function of fluid velocity, u_{avg} , for (a) air (20°C) and (b) water (20°C) by using the friction data for woven-screen matrices	50
Figure 2 11	$Re'/Re = (1 - F\phi)/F\phi$ versus Re_{max} for graphite foam ($D=300\text{mm}$) with porosity $\phi=78\%$, 80% , and 82%	54

Figure 2 12:	Experimental configuration of the heat exchanger system (Tee, 2000).....	56
Figure 2.13:	Overall convective heat transfer coefficient as a function of mean pore diameter, D , of graphite foam with a porosity of 80%, for air (20°C) with different velocities	58
Figure 2 14:	Overall convective heat transfer coefficient of graphite foams with mean pore diameter, $D = 300 \mu\text{m}$ and porosities of 78% , 80%, 82% as a function of average free stream velocity, u_{avg} , for air (20°C)	59
Figure 2.15:	Overall convective heat transfer coefficient of graphite foams with mean pore diameter, $D = 250\mu\text{m}$, $300\mu\text{m}$, and $350\mu\text{m}$, and porosity of 80% as a function of average free stream velocity, u_{avg} , for air (20°C) .	60
Figure 2.16:	Overall convective heat transfer coefficient of graphite foam with porosity of 80%, and a mean pore diameter, $D = 300 \mu\text{m}$ as a function of average free stream velocity, u_{avg} , for air with different mean bulk temperature	62
Figure 2.17:	Overall convective heat transfer coefficient as a function of flow rate for heat exchanger using graphite foams	63
Figure 2.18:	Overall convective heat transfer coefficient as a function of mean pore diameter, D , of graphite foam with a porosity of 80%, for water (20°C) with different velocities..	64
Figure 2.19:	Overall convective heat transfer coefficient of graphite foams with mean pore diameter, $D = 300 \mu\text{m}$ and porosities of 78% , 80%, 82% as a function of average free stream velocity, u_{avg} , for water (20°C)	65
Figure 2.20:	Overall convective heat transfer coefficient of graphite foams with mean pore diameter, $D = 250\mu\text{m}$, $300\mu\text{m}$, and $350\mu\text{m}$, and porosity of 80% as a function of average free stream velocity, u_{avg} , for water (20°C)	66
Figure 2.21.	Overall convective heat transfer coefficient of graphite foam with porosity of 80%, and a mean pore diameter, $D = 300 \mu\text{m}$ as a function of average free stream velocity, u_{avg} , for water	

	with different mean bulk temperature	67
Figure 5.1:	Geometric model representing a single circular cylindrical fiber embedded in a concentric circular cylindrical matrix.....	81
Figure 5.2:	Two-dimensional projection of a single circular cylindrical fiber embedded in a concentric cylindrical matrix.....	82
Figure 5.3:	FEA model considering only one quarter of the actual physical model, with the deformed shape shown by the dashed lines.....	86
Figure 5.4:	Two-dimensional eight-node, biquadratic axisymmetric element in ABAQUS.....	87
Figure 5.5	A typical mesh generated by PATRAN, employed in the present FEA	89
Figure 5.6	Effective Longitudinal Young's modulus, E_c , of 20%-SiC/Al composite, as a function of fiber aspect ratio, l/a	93
Figure 5.7:	Effective Longitudinal Young's modulus, E_c , of 10%-SiC/Al composite, as a function of fiber aspect ratio, l/a	94
Figure 5.8:	Effective Longitudinal Young's modulus, E_c , of 30%-SiC/Al composite, as a function of fiber aspect ratio, l/a	95
Figure 5.9:	Effective Longitudinal Young's modulus, E_c , of SiC/2124 composite, as a function of fiber volume fraction, f , for fiber aspect ratio, $l/a = 1.6$	97
Figure 5.10:	Effective Longitudinal Young's modulus, E_c , of SiC/6061 composite, as a function of fiber volume fraction, f , for fiber aspect ratio, $l/a = 3$	98
Figure 5.11:	Effective Longitudinal Young's modulus, E_c , of SiC/8090 composite, as a function of fiber volume fraction, f , for fiber aspect ratio, $l/a = 4$	99
Figure 5.12	Effective Longitudinal Young's modulus, E_c , of 20%-SiC/Al composite, as a function of fiber aspect ratio, l/a , for $l/a = l'/b$	100

NOMENCLATURE

Chapter 1~3:

A_c	minimum free flow cross-sectional area
A_{cell}	internal surface area of a unit cell
A_{ch}	area of the spherical end caps on the hexagonal faces
A_{fr}	frontal area of the hexagonal surface
A_s	surface area of the sphere
A_{total}	total surface area of the foam
a	length of the unit cell
$a_{hex} (a_{sq})$	distance between two parallel hexagonal (square) faces of the cell
B	constant coefficient in the power law relations
b	thickness of the foam block
C_1	constant term that depends on the microstructure of the cell
C_2	correction factor for a cell shape
c, c'	constant terms depends on fluid turbulence, foam morphology, etc
c_p	fluid specific heat
D	mean pore diameter of the foam and diameter of spherical void
D_h	hydraulic diameter
D_{hex}	diameter of circle on hexagonal face of the tetrakaidecahedron cell
d	diameter of circular cylinder strut/reference diameter
f	friction factor

F	modified Reynolds number coefficient
h	convective heat transfer coefficient
$h_{overall}$	overall convective heat transfer coefficient
k_f	thermal conductivity of the fluid
k_s	thermal conductivity of the solid
L	length of the unit cell or edge length of each side of the tetrakaidecahedron cell
L_p	total length of the foam in the flow direction
m	an exponent in the power law
\dot{m}	mass flow rate per unit width
N_s	total number of cylinders per unit thickness inside the slice of foam
Nu	Nusselt number
n	direction normal to the contacting surface/ an exponent in the power law
p_o, p_e	inlet and outlet pressure of cooling fluid, respectively
Pr	Prandtl number
p_w	normal stresses due to the pressure gradient
$Q_s(x)$	energy carried by the fluid at x
Q_s^{Total}	total heat flux transferred in the graphite foam
q	heat transfer rate at the cylinders
q_w	heat transfer rate at the wall

\dot{q}	heat flux
Re	Reynolds number
Re'	modified Reynolds number
Re_{max}	maximum Reynolds number
St	Stanton number
T	temperature of the cylinder
T_{∞}	temperature of the free stream flow
T_l	uniform temperature of the top surface of foam block
T_b	mean bulk temperature of the fluid
T_o, T_e	inlet and outlet temperature of cooling fluid, respectively
T_f, T_s	temperature distribution in the fluid and in the solid
$T_f(0), T_f(L_p)$	inlet and outlet cooling fluid temperature, respectively
T_w	temperature of the wall
u_{avg}	average free stream velocity of the fluid
u_{max}	maximum fluid velocity
u_o	cooling fluid initial velocity
u	free stream velocity of the fluid
V_{cell}	unit cell volume
V_{ch}	volume of spherical end caps on hexagonal faces
V_{void}	unit void volume
W_p	width of plate
x, y, z	Cartesian coordinates

X, Y, Z	cylindrical strut parallel to x-, y-, or z- direction
α_A	surface area density of the foam
ΔP	pressure drop across the foam
ΔT_m	logarithmic mean temperature difference
Δx	thickness of the foam slice
ϕ	foam porosity
η	net surface area
μ	average fluid viscosity
μ_f	fluid viscosity coefficient
μ_w	fluid viscosity near the wall
ν_f	fluid kinematic viscosity
ρ	foam relative density
ρ_f	fluid density
ρ^*	foam density
ρ_s	graphite strut density

Chapter 4~6:

a	radius of cylindrical fiber
A_i	area of the i th element of the composite end
A_{total}	total area of the composite end
b	radius of cylindrical matrix

E_c	effective longitudinal Young's Modulus of the composite
E_f	fiber Young's Modulus
E_m	matrix Young's Modulus
f	fiber volume fraction
l	half-length of the cylindrical fiber
l'	half-length of the cylindrical matrix
p	representative volume element factor
r, θ, z	cylindrical coordinates
u_r, u_θ, u_z	radial, tangential, and axial displacement components
u^0	uniform displacement prescribed on the top surface of the composite
$\varepsilon_r, \varepsilon_\theta, \varepsilon_z$	radial, tangential, and axial strain components
$\varepsilon_r, \varepsilon_\theta, \varepsilon_z$	radial, tangential, and axial strain components
$\bar{\varepsilon}_z$	average normal strain of the composite
$\sigma_r, \sigma_\theta, \sigma_z$	radial, tangential, and axial stress components
$\bar{\sigma}_z$	average axial stress on the top surface of the composite
$\tau_{rz}, \tau_{r\theta}, \tau_{\theta z}$	shear stress components
ν_f	fiber Poisson ratios
ν_m	matrix Poisson ratios

CHAPTER 1

INTRODUCTION ON GRAPHITE FOAM

Two analytical models for predicting the overall convective heat transfer coefficient of porous graphite foam developed at the Oak Ridge National Laboratory (ORNL) are established in the present work. The models are based on two different viewpoints, i.e., the foam may be considered as an aggregation of solid bodies or an aggregation of flow passages. Geometric models are developed to account for the foam morphology properly. The results of the tetrakaidecahedron cell model agree well with the experimental results.

1.1 Background

1.1.1 Graphite foam

By using a relatively simple technique, mesophase pitch-derived graphite foams have been developed at ORNL (Klett and Burchell, 1998). The novel technique produces open-cell graphite foams with high thermal conductivities. During processing, a pitch in a mesophase state, i.e., an intermediate stage in the formation of graphitizing carbons (Shubha *et al*, 1997), is used as a precursor to assure the formation of graphitic struts or ligaments (Hager and Lake, 1992; Sandu and Hager, 1992). Two kinds of mesophase pitch-derived graphite foams have been produced by this novel method, see Table 1.1 for the properties of the foams. In comparison with other thermal management materials,

Table 1 1: Properties of graphite foams produced from different precursors (Klett *et al* , 1999a).

Graphite Foam	Density (kg/m ³)	Mean Pore Diameter (μm)	Overall Thermal Conductivity (W/mK)
ARA24	550	275	50 – 187
Conoco	600	60	40 – 135

the mesophase pitch-derived graphite foam exhibits a high isotropic thermal conductivity and a low density, see Table 1.2 (Klett *et al* 2000a). It is noted that the specific thermal conductivity, which is the ratio of the thermal conductivity to specific gravity (i.e. the ratio of the density of the material to the density of water), of the graphite foam is significantly greater than those of the conventional thermal management materials. Table 1 2 shows that the specific thermal conductivity of graphite foam is more than seven times greater than that of copper and six times greater than that of aluminum, which is one of the most popular materials for heat sinks. Traditionally, the graphite foam has a fatal shortcoming of low strength, and thus can't be used as core material for heat exchangers. The novel processing technique developed at ORNL improves the strength of the graphite foam up to 10 times by impregnating the graphite foam with

Table 1.2 Thermal properties of mesophase pitch-based graphite foams compared with those of traditional thermal management materials (Klett *et al* , 2000a).

Material	Specific Gravity	Thermal Conductivity (W/m-K)		Specific Thermal Conductivity (W/m-K)	
		In-plane	Out-of-plane	In-plane	Out-of-plane
Mesophase pitch-derived graphite foam	0.56	187	187	334	334
Copper [†]	8.90	400	400	45	45
EWC-300/Cyanate ester resin [†]	1.72	109	1	63	0.58
Aluminum [†]	2.77	150	150	54	54
Aluminum honeycomb [#]	0.19	--	10	--	53
Aluminum foam (Steiner <i>et al</i> , 1997)	0.50	12	12	24	24

[†] Amoco Product Literature (1997)

[#] Hexcel Product Data Sheet (1997)

epoxy resins to form composites or by densifying the graphite foam with chemically vapor deposited graphite. Thus, the graphite foam becomes comparable with commercial thermal management panels (Klett, 1999b). The proprietary method is fairly versatile in the sense that the pore size and the foam density can be controlled and adjusted easily (Klett and Burchell, 1998).

As it is indicated in Figure 1.1, the mesophase graphite foam cell is made up of an interconnecting network of graphitic struts (cell walls), open pores, and strut junctures (Klett, 1999b). Most of the graphite layers are oriented parallel to the cell walls and are highly aligned along the direction of the strut or ligament (Klett *et al* , 2000a). It is noted that there are predominately open, interconnected pores within the foam cells, which resemble the shape of a sphere. Also worthy of mention is that the graphite struts for the mesophase pitch-derived graphite foam are relatively thicker and the foam has less open pores than the commercially available glassy graphite foam, which is shown in Fig 1.2.

As a result of a high thermal conductivity and a large amount of contacting surface areas between pores and the cooling fluid, the graphite foams exhibit high overall heat transfer coefficients when used as a core material in heat exchangers or heat sinks. However, the mechanical pumping power that is necessary to overcome the pressure drop mainly due to cooling fluid friction across the foam is relatively high at high flow rates in comparison with conventional heat exchanger systems (Klett and Burchell, 1998). Therefore, the interaction between the pressure drop and the heat transfer coefficient of graphite foam is essential to be understood and analyzed in order to optimize the heat exchanger using graphite foam as the core material.

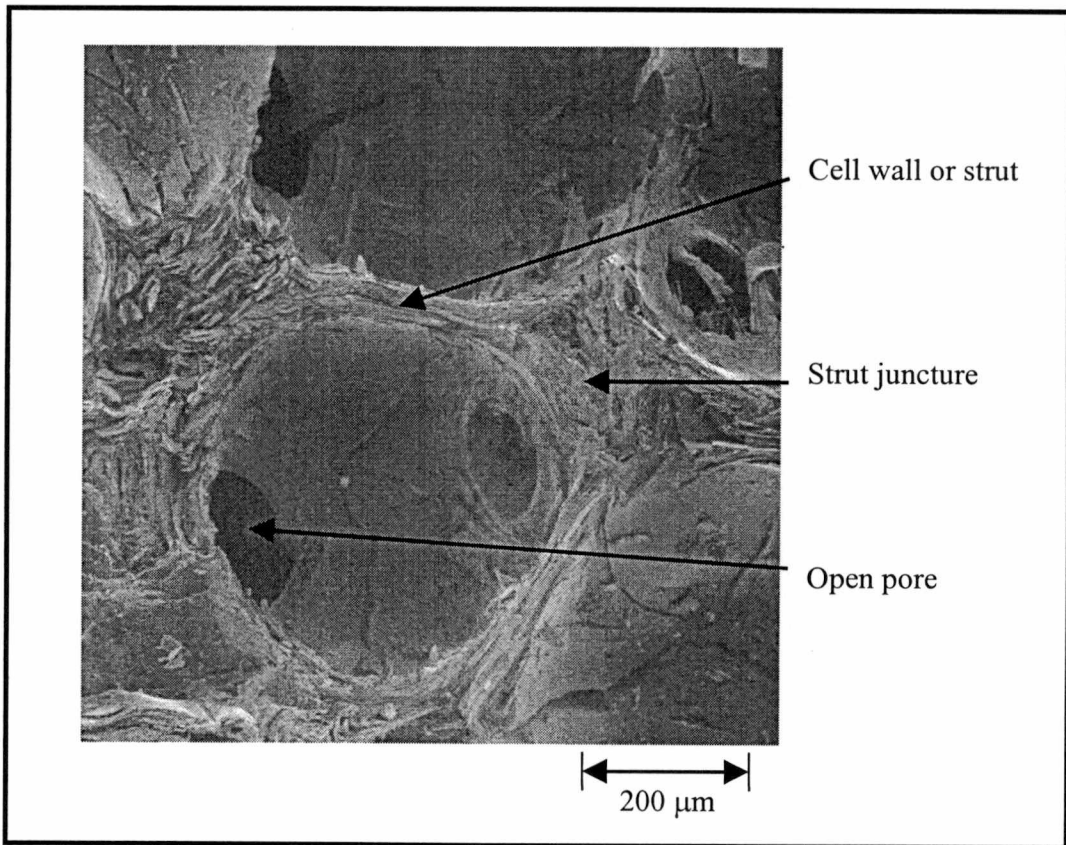


Figure 1.1: Typical microstructure of mesophase pitch-derived graphite foam (Klett, 1999b).

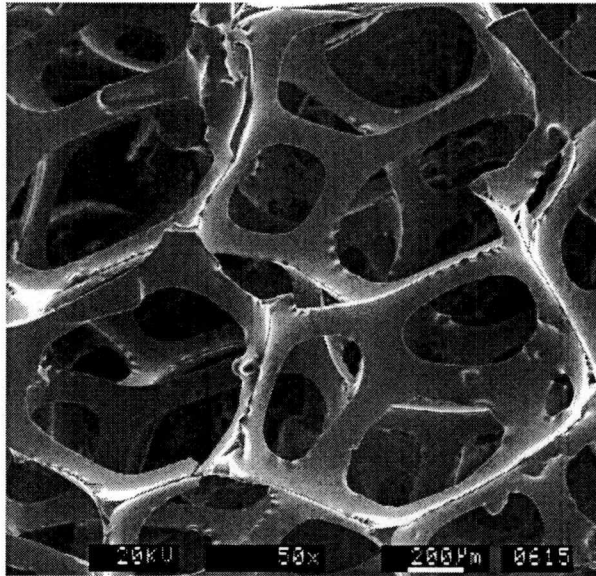


Figure 1.2: Reticulated glassy graphite foam produced by ERG Corporation (Klett, 1999b).

1 1 2 Convective heat transfer

Convective heat transfer is the heat transport process between layers in a fluid in motion and/or between a fluid in motion and a contacting surface at different temperatures Nusselt (1915) points out:

In the literature one finds very often the statement that the heat transfer from a solid body to the surrounding follows in general three different mechanisms. radiation, heat conduction and convection It is said that, either by buoyancy force or by forced air flow, permanently cold eddies of the air contact the surface of the heated body and heat is removed from the surface By the distinction between heat transfer through conduction and convection it is suggested that these are two independent mechanisms Consequently, one might conclude that heat could be transferred by convection only without the help of thermal conduction However, this is not true The truth is, that the basic equation of Fourier $dQ = -k(\partial T / \partial n)dAdt$ applies to both heat conduction and convection If the thermal conductivity, k , of the ambient medium is zero, there would be no heat transfer, neither through conduction nor through forced convection. If, however, the thermal conductivity of the ambient medium is not zero, then all the heat, except that transferred by radiation, will be transferred through conduction However, the amount of heat transferred may be increased by the fact that the surrounding medium has a certain flow velocity and this velocity affected that $\partial T / \partial n$ at the surface of the body

That is, only two mechanisms of heat transfer can be distinguished physically: heat transfer by conduction, and heat transfer by radiation. In the first case the carrier of heat energy is the matter; in the latter case the heat energy is carried by electromagnetic waves. Nevertheless, the terms *conduction*, *convection* and *radiation* are so commonly used that they are also referred to in the present work.

The convective heat transfer behavior can be characterized by the Nusselt number, Nu , defined by

$$Nu = \frac{hd}{k_f} \quad (1.1)$$

where, k_f is the thermal conductivity of the fluid, d is a reference (characteristic) diameter; and h is the convective heat transfer coefficient given by

$$h = -\frac{k_f (\partial T_f / \partial n)_w}{T_w - T_\infty} \quad (1.2)$$

or

$$h = -\frac{k_s (\partial T_s / \partial n)_w}{T_w - T_\infty} \quad (1.3)$$

where k_s is the thermal conductivity of the solid; T_f and T_s are the temperature distribution in the fluid and in the solid, respectively; T_∞ is the temperature of the free stream flow, T_w is the temperature of the wall, the subscript w implies that the derivative is evaluated at the contacting surface (wall), and n denotes the direction normal to the contacting surface. The convective heat transfer coefficient has the unit $W/(m^2 \cdot K)$ in SI system. In essence, the Nusselt number is a measure of the ratio of the magnitude of the convective heat transfer rate to the magnitude of the heat transfer rate for pure conduction. The Nusselt number can be expressed by (see, for example, Kakac, *et al*, 1987):

$$Nu = c Re^m Pr^n \left(\frac{Pr}{Pr_w} \right)^p Tu^{0.15} \quad (1.4)$$

where, c , m , n , and p are constants. The Reynolds number, Re , is defined by

$$Re = ud / \nu_f \quad (1.5)$$

where, u is a reference (characteristic) velocity, and ν_f is the kinematic viscosity of the flow. The Reynolds number is the ratio of the magnitude of the inertia force to the magnitude of the viscous force in the flow. The Prandtl number, Pr , is defined by

$$Pr = c_p \mu_f / k_f \quad (1.6)$$

where c_p and μ_f are the specific heat and the coefficient of viscosity of the fluid, respectively. The Prandtl number is the ratio of the kinematic viscosity to the thermal diffusivity of the fluid, and is a measure of the relative efficiency of the fluid as a conductor of momentum and energy. The Prandtl number of the fluid at the wall temperature is denoted by Pr_w whereas Tu is the turbulence level in percent. Since m , n , and p are usually positive, the overall convective heat transfer coefficient thus increases as the Reynolds number and/or the Prandtl number increases.

For gases, the Prandtl number is constant and $Pr/Pr_w \approx 1$. Thus Eq. (1.4) becomes

$$Nu = c Re^m Pr^n Tu^{0.15} \quad (1.7)$$

The combination of the coefficient c with the term $Tu^{0.15}$ in Eq. (1.7) gives

$$Nu = c' Re^m Pr^n \quad (1.8)$$

where $c' = cTu^{0.15}$. It is noted that Eq. (1.8) is indeed universally valid. The coefficient c' and the exponents m and n , however, depend on the fluid turbulence, geometry of the porous medium, surface roughness, etc. For foams, the values of c' , m , and n are greatly affected by foam morphology. Thus adequate geometric models are established in the next chapter in order to predict the overall heat transfer coefficient of porous graphite foams.

1.1.3 Heat transfer coefficients

The concept of the individual convective heat transfer coefficient h , which is the proportionality constant between the heat flux \dot{q} and the temperature driving force ΔT , is not a fundamental quantity, but is introduced for convenience in the formulation of the equations. In fact, there are a number of heat transfer processes (e.g., nucleate boiling and natural convection) for which h is not independent of the temperature difference, and it would therefore seem to have no applicability of h in these cases. Nevertheless, the convenience of using h is so great and the alternatives so difficult in most cases in the estimate of heat transfer efficiency as well as in the design of heat exchangers.

For example, a major advantage of using h to quantify heat transfer rates is that the individual h of two different fluids exchanging heat may be utilized to relate the local rate of heat transfer to the local temperature difference between the two fluids (Hewitt, 1990). On the other hand, the overall heat transfer coefficient of foam depends not only on the individual heat transfer coefficient of the fluid and solid, but also on the thermal conductivity of the foam, and this is the exact reason why mesophase pitch-derived open-cell graphite foams with high thermal conductivities developed at ORNL may be promising materials for heat exchanger applications.

1.2 Literature Review

As the design of heat exchanger involves the consideration of both the heat transfer rates between the fluids and solids, and the mechanical pumping power expended to overcome the fluid friction and to move the fluids through the heat

exchanger, the heat transfer coefficient together with hydraulic resistance characterized by pressure drop has been studied from the very beginning of the 19th century. King (1914) studies the heat transfer and hydraulic resistance of a single cylindrical tube under cross flow. Thoma (1921) further discusses the effects of the geometry of a bank of tubes on their heat transfer and flow resistance behavior and concludes that a tube is subjected to higher heat transfer per unit area (i.e. heat flux) when it belongs to a bank of tubes than it works as a single tube, which demonstrates that the heat flux is a function of the number of rows and the arrangement of tubes. Žukauskas (1987) presents the heat transfer and pressure drop of fluids flowing through a single cylindrical tube and banks of tubes of various arrangements, including the heat transfer between tubes in cross flow. Extensive experimental data with Prandtl number ranging from 0.7 to 500 and Reynolds number ranging from 1 to 2×10^6 are analyzed. Žukauskas (1987) concludes that it is the maximum velocity, not the average velocity, of the fluid should be employed as the reference in computing the Prandtl and Reynolds numbers, as it reflects the actual resistance with sufficient accuracy, except for closely spaced banks.

Antohe *et al.* (1996) develop a microporous heat exchanger to cool high-power electronics using a mechanically compressed porous aluminum layer to improve the heat transfer and to provide relatively uniform cooling. The hydraulic characteristics of the porous aluminum layer are obtained experimentally and are used in the numerical simulations of a real microporous heat exchanger.

Locke (1950) develops a transient test technique for determining heat transfer characteristics of the low Reynolds-number flows. Coppage (1952) then utilizes Locke's

technique in determining the heat transfer characteristics of porous media formed from stacked woven-wire screens. The results, valid for $5 < Re < 1000$, are extended up to $Re = 10^5$ by Tong (1956) using a different transient technique and crossed-rod matrices. London and his co-workers (London *et al.*, 1960; London *et al.*, 1970, London and Shah, 1973; and Kays and London, 1984) conduct extensive experiments on the heat transfer and flow friction characteristic of crossed-rod matrices, woven-screen matrices, and porous glass-ceramics matrices. The experiments investigate convective steady-state isothermal flows, in which the pressure drop is measured for essentially constant-density airflows. All experimental results for these matrices have been presented graphically in terms of a non-dimensional friction factor, f , as a function of the Reynolds number, for the fluid flow. The porosities of the crossed-rod and woven-screen matrices investigated range from 60% to 83%, and the Reynolds number ranges from 5 to 100,000, which covers both the laminar flow region and the transition region. No correlation of the flow friction data with the *entire* range of Reynolds number is successfully obtained (Coppage and London, 1956, Tong and London, 1957; and London *et al.*, 1960). When the porosity of the porous matrix exceeds 70%, the in-line crossed-rod configuration has the lowest for a constant Reynolds number while the staggered crossed-rod configuration shows the highest friction factor. The behavior of woven-screen matrix is similar to that of the random crossed-rod configuration. In addition, the friction behavior of the inline and staggered configurations at high porosities agrees well with the behavior of comparable tube-bank geometries. When the porosity approaches unity, the friction behavior of the inline and staggered configurations, by extrapolation, is consistent with

the aerodynamic-drag behavior of single cylinders (London *et al.*, 1960)

For the porous glass-ceramic matrices with straight triangular, hexagonal, or circular passage surfaces, the porosities investigated cover the range of 64% to 81% and the Reynolds number ranges from 60 to 1000. The passages exhibit heat transfer surface area densities ranging from 1300 to 2400 ft²/ft³, corresponding to passage counts of 526 - 2215 passages/in². As a result, one finds that the glass-ceramic with hexagonal passages has its advantages over the triangular passage geometry, which is commonly used for gas turbine regenerators in vehicles. For an instance, a 30% increase in heat transfer performance, along with a 13% reduction in pressure drop for the same disc envelope geometry tested was gained (London *et al.*, 1970, London and Shah, 1973)

Hunt and Tien (1988) examine the heat transfer of non-Darcy flow in high-porosity fibrous media. Several types of fibrous medium, including carbon, nickels, and aluminum, are tested under forced convection, while different parameters, such as permeabilities, porosities, and thermal conductivities, are experimentally and analytically studied. Traditional analyses based on porous media usually utilize Darcian or slug flow models (Vafai and Tien, 1981) and neglect the non-Darcian effects, such as the viscous shear force along solid boundaries, the inertial convective force, and thermal dispersion. However, because the fluid in essence moves in tortuous paths throughout the porous medium and recirculates at the back of the solid fibers, the convective or inertial effects increase with an increase in Reynolds number, thus yields an increase in pressure drop across the medium. On condition that a temperature or a concentration gradient occurs across the fibers, the recirculation or dispersion will mix the fluid particles and increase

the net transport. Hunt and Tien (1988) consider these effects by using a volume-averaging process. The momentum equation is obtained by volume averaging the Navier-Stokes equation and relating the drag force caused by the presence of the solid phase to the Darcian force. However, the governing equations rely on additional empirical relations for closure as microscopic phenomena such as local recirculation or dispersion are eliminated by the averaging method.

Huang and Vafai (1993) analyze the relationship between the flow pattern and heat transfer characteristics in multiple porous block structures. A general flow model that accounts for the effects of the impermeable boundary and inertial effects is established to simulate the flow inside the porous region. Numerical solutions have been obtained with the aid of a stream function-vorticity by using a finite-difference method. The effects of Darcy's number, Reynolds number, Prandtl number, the inertia parameter, and other pertinent geometric parameters are thoroughly explored to predict the hydraulic resistance of porous media. It is reported that two distinct boundary layers exist for the velocity field, while only one boundary layer is observed for the temperature field. Huang and Vafai conclude that the presence of a porous block near an impermeable boundary significantly changes the convection characteristics.

Recent development in heat exchangers has been directed towards compactness, which is dictated, in part, by high power electronics that demand operation at power densities above 10^7 W/m². Lu *et al.* (1998) explore the usage of open-cell metallic foams as compact heat exchangers, exploiting convective cooling. A simple cubic unit cell consisting of heated slender cylinders based on existing work on convective cross-flow

through cylinder banks is established for metallic foams. The energy flow due to forced convection and conduction through ligaments of the cellular foam is considered in the model. The overall heat transfer coefficient of the heat exchanging system is calculated with the aid of analogy between flow through the foam and that across a bank of cylinders, the resulting pressure drop across the foam is determined, and the optimum foam properties for the best heat transfer performance are suggested. Since the model, which is based on a cross flow across a bank of cylinder, is idealized to reduce the complexity of forced convective flow across open-celled foam, it may oversimplify the transport phenomenon in metallic foams consisting of non-circular, possibly sharp-edged ligaments. The assumptions made in order to analyze the heat transfer in disordered, porous materials likely lead to an overestimate of the actual level of heat transfer (Tien and Vafai, 1990). The assumption that the ligaments in all directions contribute equally to the local heat transfer seems to be one of the reasons to cause the substantial quantitative discrepancies (Bastawros *et al.*, 1999). Nevertheless the trends of heat transfer predicted by the model are in reasonable agreement with aluminum foams (Lu *et al.* 1998, Bastawros *et al.*, 1999).

Bastawros *et al.* (1999) present experimental measurements of the heat transfer and pressure drop characteristics of open-cell metallic foams subjected to transverse airflows. Two models are developed with their appropriateness being assessed by measurements. The model for effective properties is based on volume averaging techniques (Koh and Colony, 1974; Vafai and Sozen, 1990; Amiri and Vafai, 1994), and allows extrapolation to cellular solids with various densities and cell sizes. The other

model includes a heat constriction effect and utilizes an equivalent fin array, similar to a bank of cylinder to study the effects of various interfaces while accounting for the anisotropy of unit cell.

1.3 Nature of the Problem

Modeling of forced convection in porous media has been extensively applied to heat exchanger simulation and design. The modern emphasis on heat transfer augmentation, and the more recent demand on miniaturization in the cooling of electronics, have led to the development of compact devices with much smaller features than those in the past. Graphite foams receive extensive attention as high-efficiency heat sinks or compact heat exchangers in light of high specific thermal conductivities and heat transfer coefficients, despite the fact that the mechanical pumping power necessary to overcome the pressure drop due to cooling fluid friction across the foam is relatively high at high flow rates in comparison with conventional heat exchanger systems (Kays and London, 1984). The overall heat transfer coefficient and pressure drop together with the flow field in the graphite foam subjected to cross flow are studied in the present work in order to optimize the performance of foam as a core material for cooling heat exchanger. The long-term goal of graphite foam development is to optimize the heat transfer rate while maintaining a relatively lower pressure drop across the foam.

Most of the existing studies on heat transfer in a porous medium consider Darcy's Law, which is only valid for creeping flows through an infinitely extended uniform medium with Reynolds numbers less than about ten (Tien and Vafai, 1990, Bejan, 1993).

For open-celled metallic or graphite foams, the fluid velocity is usually high and the porous medium is bounded, rendering the assumption of Darcian flow and local thermodynamic equilibrium invalid (Lu *et al.*, 1998). In the present work, in order to determine the relationship between the foam morphology and the heat transfer characteristics for forced convective flows through open-celled graphite foam, two geometric models, namely, the cubic cell model and the tetrakaidecahedron cell model, are developed to simulate the foam microstructure and convective heat transfer characteristics. While the cubic cell model regards the graphite foam as an assemblage of cylinders, the tetrakaidecahedron model is based on the view that the graphite foam provides an aggregation of flow passages.

The results obtained from the models are compared with the experimental measurements conducted at ORNL (Tee, 2000) Although they involve approximations and assumptions to reduce the complexity of forced convection flows across porous foam, the models capture the approximate functional dependence of micro-structural variables, such as porosity, pore size, and fluid velocity, on heat transfer in foam.

CHAPTER 2

ANALYTICAL MODELING ON OVERALL CONVECTIVE HEAT TRANSFER COEFFICIENT OF GRAPHITE FOAM

2.1 Cubic Cell Model

2.1.1 Geometrical representation

A cubic cell model consisting of slender circular cylinders as edges is employed to model the energy flow due to forced convection as well as conduction in cellular foams. As it is indicated in Fig. 2.1, a block of foam, made up of equal-sized, aligned cubic cells, is sandwiched between two plates with length L_p and width W_p . A uniform temperature T_1 is prescribed on the top plate, which is assumed to be thin and to have a high thermal conductivity so that the through-thickness heat conduction may be neglected. It is further assumed that the two ends that are perpendicular to the y -axis at $y = W_p/2$ and $-W_p/2$, and the bottom plate at $z = b$ are thermally insulated. A cooling fluid with an initial velocity u_0 , high pressure p_0 , and temperature T_0 is forced into the foam at the inlet, $x = 0$, and exits at the outlet, $x = L_p$, with a lower pressure p_e , and a higher temperature T_e . It is noted that the configuration shown in Fig. 2.1 can be regarded as, due to symmetry, the upper half of that is shown in Fig. 2.2 where both the top and bottom plates are kept at the uniform temperature T_1 , and the distance between the two isothermal plates is $2b$. Each cubic unit cell is made up of twelve circular cylinders with a diameter d and a length a ; see Figure 2.3. For simplicity, the cylindrical

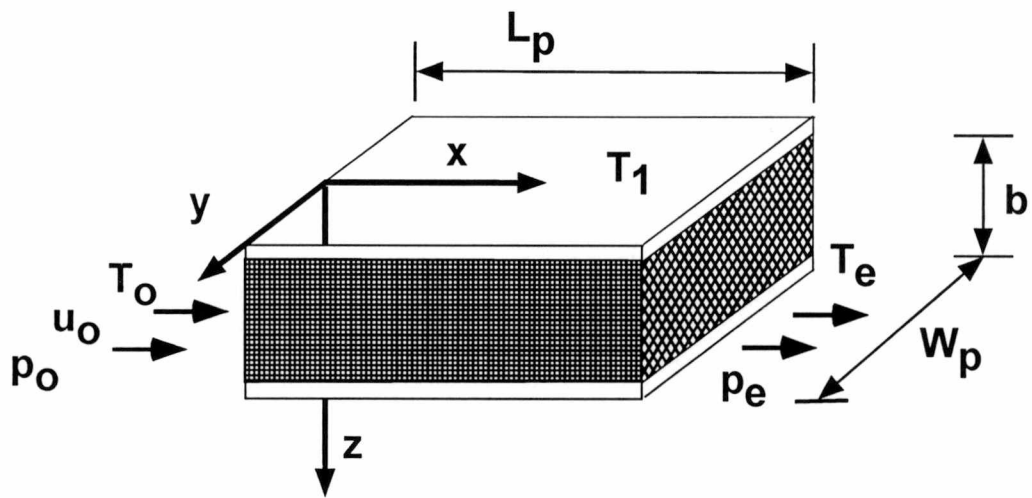


Figure 2.1: Forced convection in porous graphite foam.

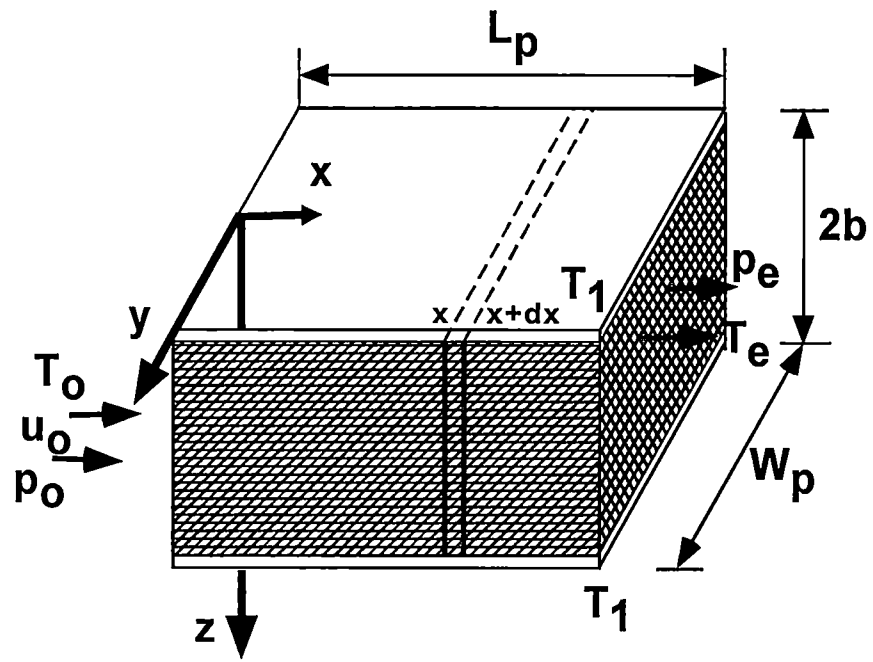


Figure 2.2: Modified domain of forced convection in porous graphite foam.

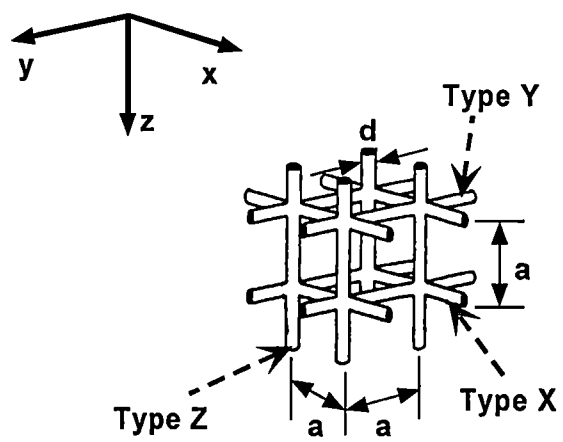


Figure 2.3: Cubic unit cell consisting of struts with a circular cross-sectional area (Lu *et al*, 1998)

struts making up the cell edges are assumed to be parallel to the x-, y- or z-coordinate axis, and are denoted by cylinders of type X, Y and Z, respectively. The present work considers (1) a single cylinder of type Z with temperature T_1 specified on its top and bottom, (2) a bank of cylinders of type Z in cross-flow, and (3) graphite foam with cubic cells in cross-flow.

The properties of foam depend strongly on its relative density, ρ , which is the ratio of the density of the foam, ρ^* , to that of the struts, ρ_s , and can be related to the porosity, ϕ , by

$$\rho = \frac{\rho^*}{\rho_s} = 1 - \phi \quad (2.1)$$

For all of the open-cell foams, the relationship between ρ and the ratio of cylinder diameter to length, d/a is approximately governed by (Gibson and Ashby, 1997):

$$\rho = C_1 \left(\frac{d}{a} \right)^2 \left[1 - C_2 \left(\frac{d}{a} \right) \right] \quad (2.2)$$

where C_1 is a constant that depends on the microstructure of the cell and can be experimentally determined, and C_2 is a correction factor for a given cell shape, and is significant only if ρ is greater than 0.2. For an open *cubic* cell consisting of slender

cylindrical struts, the normalized diameter of the cylinder, d/a , may be approximately related to the relative density by (Lu *et al* , 1998):

$$\rho \approx \frac{3\pi}{4} \left(\frac{d}{a} \right)^2 \quad (2.3)$$

Besides, the surface area density, α_A , for an open cubic cell can be given by (DeHoff and Rhines, 1968)

$$\alpha_A \equiv \frac{A_s}{V} = \frac{4\rho}{d} \quad (2.4)$$

where A_s is the surface area of the foam and V is the volume of the foam. Equation (2.4) holds for any space filling cubic unit cell having the same relative density and cylindrical strut cross-section (DeHoff and Rhines, 1968), and is confirmed by Bastawros *et al* (1999), who used computed tomography to measure the surface area density of aluminum foams. Thus, the total surface area per unit width, A_s/W_p , of a segment of foam with height $2b$ and length L_p , consisting of cubic cells, is approximately given by combining Eq. (2.3) and (2.4) (Lu *et al* , 1998):

$$\frac{A_s}{W_p} \approx \rho^{1/2} \left(\frac{4\sqrt{3\pi} L_p b}{a} \right) \quad (2.5)$$

The surface area density of the foam, an important parameter for heat exchange systems, is related to ρ and a by, again, combining Eq (2.3) and Eq. (2.4)

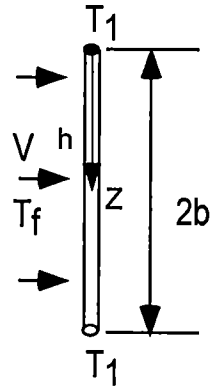
$$\alpha_A \equiv A/V \approx \rho^{1/2} \left(\frac{2\sqrt{3\pi}}{a} \right) \quad (2.6)$$

A large amount of surface area, say, $\alpha_A > 700 \text{ m}^2/\text{m}^3$, is typical for gas-flow compact heat exchangers.

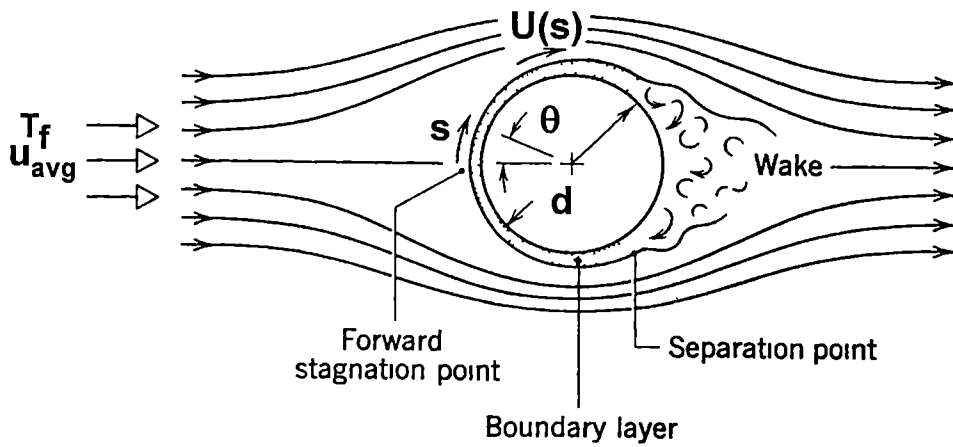
2.1.2 A single cylinder in a cross flow

The ligaments in an open-celled foam are similar in many ways to the fins common in heat exchangers. Thus a single, isolated cylinder of type Z, is first considered in Fig 2.4. For a circular cylinder of type Z (or Y) in cross flow, the characteristics of the flow depend very strongly on various parameters such as the size, and orientation of the cylinder, as well as fluid properties (Munson *et al*, 1994). For simplicity, it is assumed that the turbulent flow inside the foam is well mixed and a one-dimensional model for the fluid temperature, T_f , assumed to vary only with x , is developed. As the cylinder is considered to be slender ($d \ll a < b$), its temperature, $T(z)$, is assumed to be uniform across the cross section of the cylinder. This simplification is based on the observation that the aspect ratio d/a is typically small for most low-density, open-celled foams.

Under steady-state conditions, the variation of temperature $T(z)$ along the length



(a)



(b)

Figure 2.4: Boundary layer formation and separation on a circular cylinder in a cross flow

(a) longitudinal view, (b) cross-sectional view (Incropera and DeWitt, 1990)

of a slender cylinder is governed by (Lu *et al* , 1998)

$$\frac{d^2 T(z)}{dz^2} - \frac{4h}{k_s d} (T(z) - T_f) = 0 \quad (2.7)$$

where the Fourier law of heat conduction and Newton's law of cooling have been used, k_s is the thermal conductivity of the solid, and h is the convective heat transfer coefficient. At the cylinder surface, the heat transfer due to radiation is usually at least one order of magnitude smaller than that due to forced convection, and is thus neglected. The solution to Eq (2.7), with the boundary conditions that $T = T_1$, at $z = 0$ and $z = 2b$ (see Fig. 2.4a), is given by

$$T(z) = T_f + \frac{(T_1 - T_f) \{ \sinh[2Bi^{1/2}(2b - z)/d] + \sinh(2Bi^{1/2}z/d) \}}{\sinh(4Bi^{1/2}b/d)} \quad (2.8)$$

where the Biot number is given by

$$Bi = hd / k_s \quad (2.9)$$

By integrating Eq (2.8) from $z = 0$ to $2b$, the average temperature of the cylinder, \bar{T} , is given by

$$\bar{T} = T_f + 2(T_1 - T_f) \frac{\cosh(4Bi^{1/2}b/d) - 1}{(4Bi^{1/2}b/d) \sinh(4Bi^{1/2}b/d)} \quad (2.10)$$

The heat flux entering the cylinder at $z = 0$ and $z = 2b$ is given by

$$q = -\left(\frac{\pi d^2}{4}\right) k_s \left\{ \left(\frac{dT}{dz}\right)_{z=0} + \left(\frac{dT}{dz}\right)_{z=2b} \right\} \quad (2.11)$$

Combination of Eq. (2.8) and (2.11) gives

$$q = \pi k_s Bi^{1/2} d (T_1 - T_f) \frac{(\cosh(4Bi^{1/2}b/d) - 1)}{\sinh(4Bi^{1/2}b/d)} \quad (2.12)$$

Equation (2.12) gives the heat carried away by the cooling fluid, provided that there is no heat loss.

2.1.3 A bank of type Z cylinders in cross flow

The results obtained in the previous subsection are now applied to determine the heat transfer coefficient of cross flow over a bank of Z-type cylinders, which are uniformly arranged in the x-y plane. The heat transfer coefficient, h , is dependent on not only the fluid field and properties, but also the shape of the surface over which the fluid is flowing. The transfer of energy due to forced flow past a heated single cylinder or a bank of heated cylinders has been extensively studied, but the existing results are mainly

empirical (Lu, *et al* 1998). According to Gosse (1981), the average Nusselt number for a single cylinder in cross flow may be given by

$$Nu = c' Re^m Pr^{1/3} \quad (2.13)$$

which is a special case of Eq. (1.8) by setting $n = 1/3$.

For a bank of parallel but unconnected cylinders subjected to cross-flow, the heat transfer coefficient is still governed by the Nusselt number expressed in Eq. (2.13). As the thermal entrance length resides within the first or second row of cylinders (Žukauskas, 1987a), the local heat transfer beyond the third row of cylinders is assumed to attain a uniform average value. If the reference (characteristics) velocity, u , and diameter d are chosen to be the maximum fluid velocity, which u_{max} is assumed to occur in the minimum free flow area, A_{min} , in the fluid flow, and the average diameter of the cylinder d , respectively, the overall heat transfer coefficient averaged over all the cylinder surfaces may be expressed by (Oosthuizen and Naylor, 1999)

$$h = k_f c' Pr^{1/3} \left(\frac{u_{max}}{\nu_f} \right)^m d^{m-1} \quad (2.14)$$

where k_f is the thermal conductivity of the fluid, ν_f is the kinematic viscosity of the fluid, and the coefficient c' and the exponent m are dependent on the Reynolds number and the configuration of the bank of cylinders characterized by the cylinder diameter, d , the

spacing between the cylinders, a , the number of rows of cylinders, and the flow direction. The mass conservation for an incompressible fluid flow requires (Incropera and DeWitt, 1990):

$$u_{\max} = \frac{a}{a-d} u_{\text{avg}} \quad (2.15)$$

where u_{avg} is the average free stream velocity. For cylinders arranged in a square array with at least 10 rows in each direction such that a repeatable pattern of flow established inside the bank, Holman (1989) suggests that $c' \approx 0.3$ and $m \approx 0.6$ when $a/d \geq 3$, rendering $h \propto d^{-0.4}$

2.1.4 Foam with open cubic cells

Consider a slice of foam with length Δx , located at x , (see Fig. 2.2), the energy balance requires

$$Q_s(x) = \dot{m} c_p [T_f(x + \Delta x) - T_f(x)] = N_s q + q_w \quad (2.16)$$

where $Q_s(x)$ is the total energy carried by the fluid at x , c_p is the specific heat of the fluid, N_s is the total number of cylinders per unit thickness inside the slice of foam and is given by

$$N_s = \Delta x / a^2 \quad (2.17)$$

$\dot{m} = \rho_f u b$ is the mass flow rate per unit width at the entrance to the slice of foam, with ρ_f being the fluid density at the entrance and u being the entrance velocity of the flow, and q and q_w are the heat flux into the cylinders and the fluid from both the top and bottom isothermal plates, respectively. While q is given in Eq. (2.12), q_w is given by (Lu, *et al* 1998)

$$q_w = 2\eta\Delta x h(T_1 - T_f(x)) \quad (2.18)$$

with

$$\eta = 1 - \frac{\pi}{4} \left(\frac{d}{a} \right)^2 \quad (2.19)$$

being the net surface area of the top and bottom plates per unit length per unit width excluding the cross-section areas of the cylinders. Due to relatively low Biot number (<0.02), the following relationship holds for open-celled foam (Lu *et al*, 1998)

$$\frac{\pi}{2\eta Bi^{1/2}} \left(\frac{d}{a} \right)^2 \tanh\left(\frac{4Bi^{1/2}b}{d} \right) > 10 \quad (2.20)$$

Combination of Eq (2.9), (2.12) and (2.18) gives

$$\frac{N_s q}{q_w} = \frac{\pi}{2\eta Bi^{1/2}} \left(\frac{d}{a}\right)^2 \tanh\left(\frac{4Bi^{1/2}b}{d}\right) \quad (2.21)$$

Thus, q_w can be neglected and Eq. (2.16) is thus reduced to

$$Q_s(x) = \dot{m} c_p [T_f(x + \Delta x) - T_f(x)] = N_s q \quad (2.22)$$

Substitution of Eq (2.12) and (2.17) into Eq (2.22) gives the heat transferred by the type-Z cylinders within an arbitrary slice of the sandwiched foam structure located at x :

$$Q_s(x) = 2\sqrt{\frac{\pi}{3}} \frac{\Delta x \rho^{1/2}}{a} k_s Bi^{1/2} (T_1 - T_f) \tanh(2Bi^{1/2}b/d) \quad (2.23)$$

Experimental results (Bastawros *et al* , 1999) suggest that only the cell ligaments normal to the top and bottom isothermal plates may contribute substantially to the heat flux to the fluid. Thus, integrating Eq (2.23) from 0 to L_p gives the total heat flux Q_s^{Total} transferred in the graphite foam with length L_p .

$$Q_s^{Total} = \int_0^{L_p} Q_s(x) dx \quad (2.24)$$

The overall convective heat transfer coefficient of a graphite foam-filled duct, $h_{overall}$, can be defined by (Lu, *et al* 1998)

$$Q_S^{Total} = 2L_p h_{overall} (T_1 - T_b) \quad (2.25)$$

where, Q_S^{Total} is the total heat transferred between the whole duct and the fluid and is given by

$$Q_S^{Total} = \dot{m} c_p [T_f(L_p) - T_f(0)] \quad (2.26)$$

and

$$T_b = T_1 - \Delta T_m \quad (2.27)$$

with ΔT_m being the logarithmic mean temperature given by

$$\Delta T_m = \frac{T_f(L_p) - T_f(0)}{\ln\left(\frac{T_1 - T_f(0)}{T_1 - T_f(L_p)}\right)} \quad (2.28)$$

L_p being the total length of the graphite foam in the flow direction, and $T_f(0)$ and $T_f(L_p)$ being the inlet and outlet temperature of the cooling fluid, respectively. Consequently, the overall convective heat transfer coefficient of the foam structure is given by

$$h_{overall} = \frac{Q_s^{Total}}{2L_p(T_1 - T_b)} = \left(\frac{2\rho}{3} \left(\frac{hk_s}{d} \right)^{1/2} \right) \tanh \left(2b \left(\frac{h}{k_s d} \right)^{1/2} \right) \quad (2.29)$$

2.1.5 Results

Figure 2.5 and Figure 2.6 illustrate how the variation of cell size, a , and free stream velocity u_{avg} affects the overall convective heat transfer coefficient, $h_{overall}$, of the graphite foam. It is noted that the overall convective heat transfer coefficient increases with an increase in free stream velocity or a decrease in cell size, which is in agreement with the experimental data obtained by Tee (2000). However, the predicted values of $h_{overall}$ are about 4 to 8-fold higher than those measured, see Figure 2.6. The overestimates are probably due to the oversimplification of the geometric model in order to obtain closed-form solutions. Since whether the velocities of the fluid before and after entering the graphite foam are uniform or not is still uncertain, and the temperature profiles of the fluid and the graphite foam are difficult to be determined, further studies are needed to check the validity and accuracy of the cubic cell model (Lu *et al* 1998). Another important reason may be because that the graphite foam had better be regarded as an aggregation of passages rather than struts. To this end, a tetrakaidecahedron cell model is developed in the next subsection.

2.2 Tetrakaidecahedron Cell Model

2.2.1 The unit cell

The present model assumes that a block of graphite foam is composed of three-

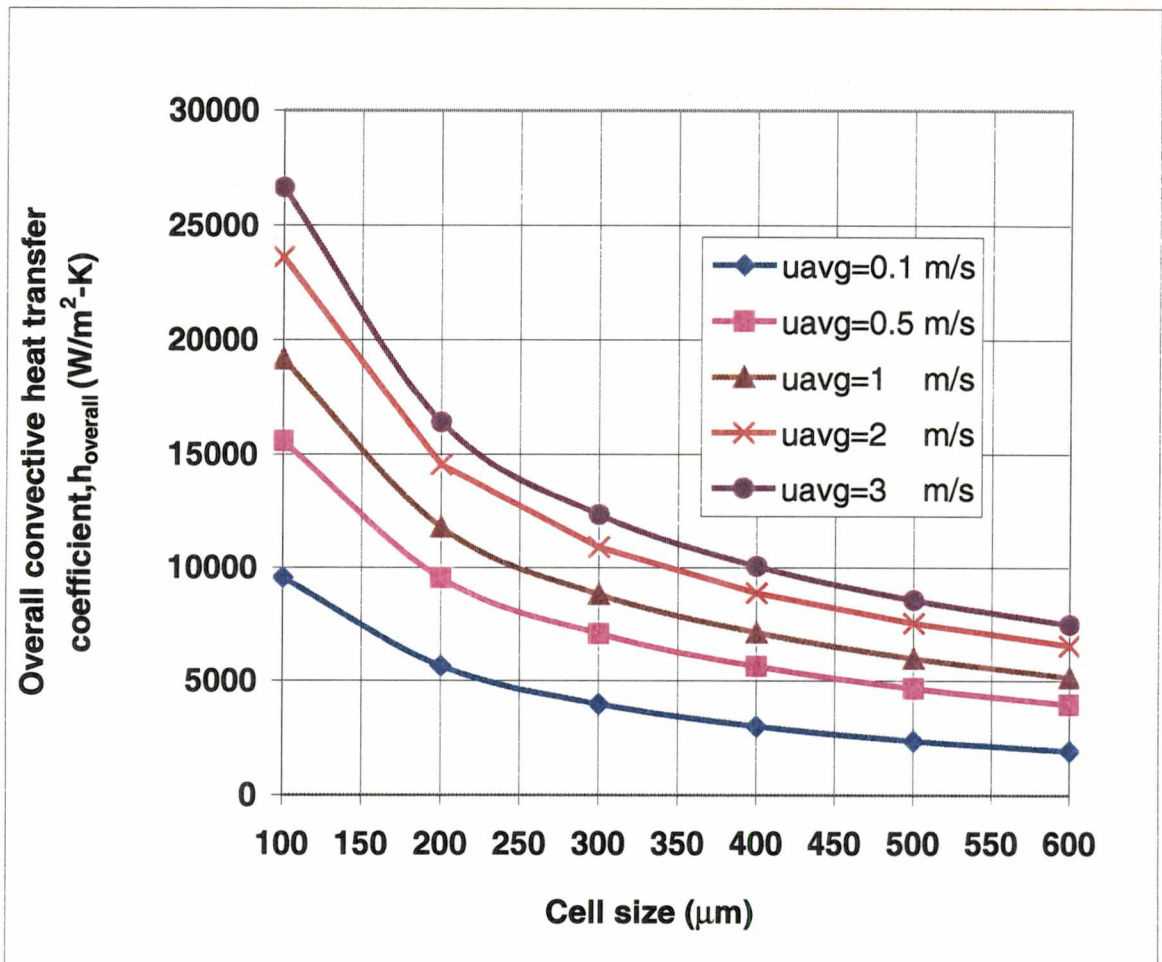


Figure 2.5: Overall convective heat transfer coefficient of graphite foam with porosity of 80% as a function of mean cell size, a , for air (20°C) with different free-stream velocities.

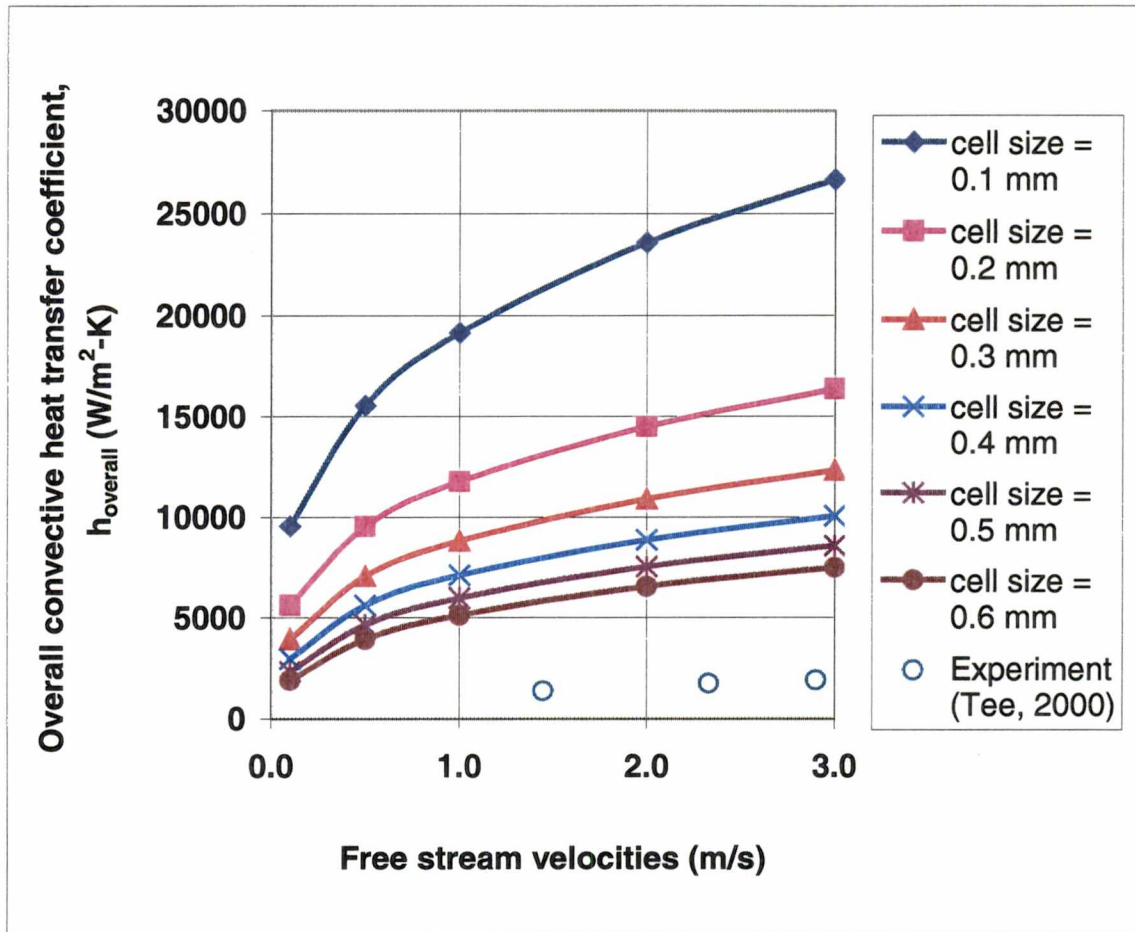
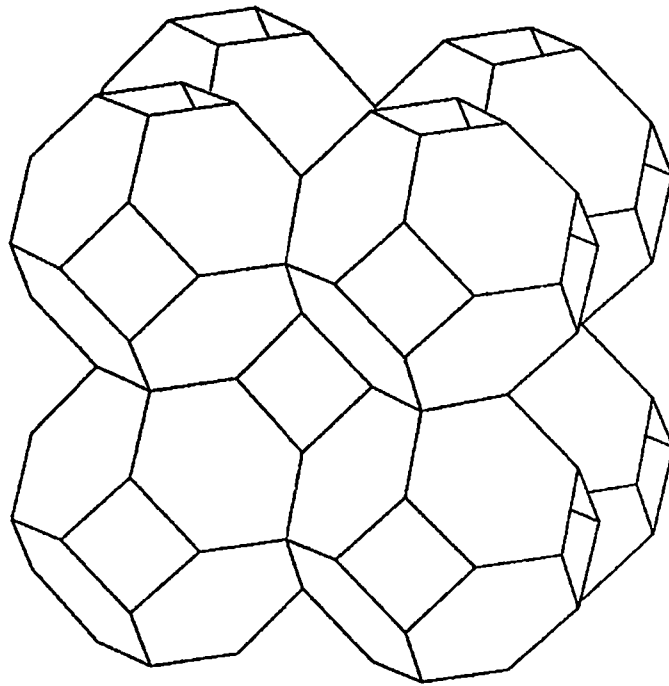


Figure 2.6: Overall convective heat transfer coefficient of graphite foam with porosity of 80% and different cell sizes as a function of free stream velocity u_{avg} for air (20°C).

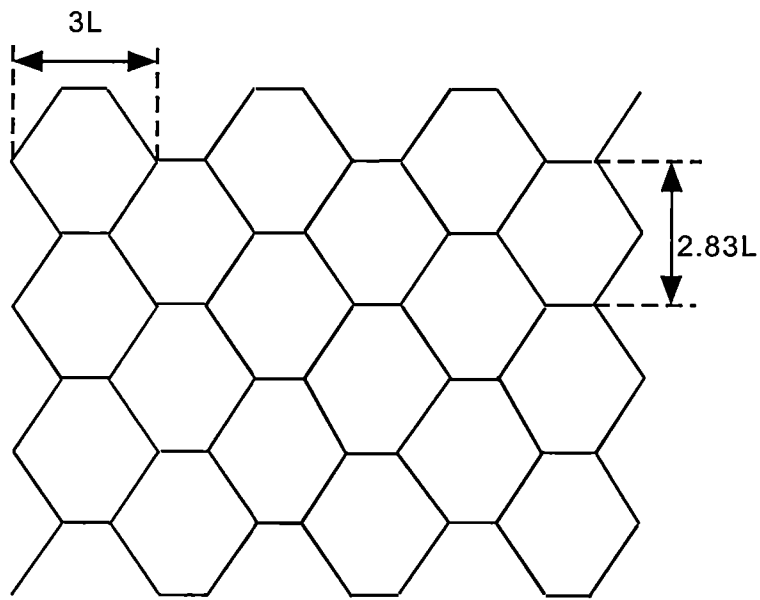
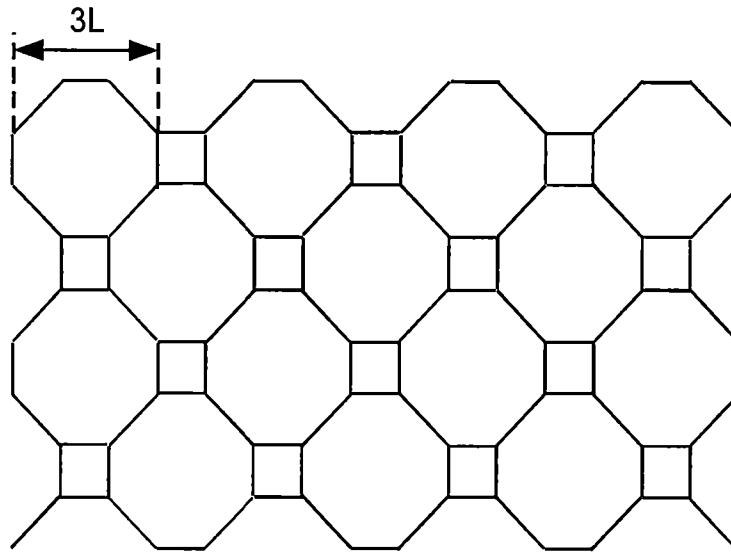
dimensional arrays of tetrakaidecahedron cells. The tetrakaidecahedron cells are packed to fill the entire space; see Figure 2.7 a, b. As indicated in Figure 2.8, the edge length of each side of the tetrakaidecahedron cell is denoted by L , a_{sq} is the distance between two mutually parallel *square* faces of the cell, a_{hex} is the distance between two mutually parallel *hexagonal* faces of the cell, and D_{hex} is the diameter of the circle on the hexagonal face. The dihedral angle between two hexagon faces is equal to $109^{\circ}28'$, and the dihedral angle between the square and hexagon face is equal to $125^{\circ}16'$ (Pearce and Pearce, 1978). Each cell has 36 edges, 6 square faces, 8 hexagonal faces, and contains a body-centered spherical void located at the center of the cell. Since the cells are open, the voids in general are interconnected with the voids in the neighboring cells (Gibson and Ashby, 1997).

A two-dimensional projection of the mid-plane of the tetrakaidecahedron cell is shown in Figure 2.9, where D is the diameter of the spherical void, i.e. the pore size. If D is larger than a_{sq} , the voids are interconnected on both the square and the hexagonal faces, and the porosities of the matrixes would be over 94%. If D is larger than a_{hex} , but less than a_{sq} , the voids would be interconnected on the hexagonal faces, the porosities of the foam would range from 69 to 94%. It is noted that the porosities of all of the graphite foams developed at ORNL are in the range of 75% to 85%. The graphite that exists in the cell is either in the form of rods at the cell edges or in the form of perforated or un-perforated plates at the faces and cell edges. The voids are interconnected with the voids in the neighboring cells.



(a)

Figure 2 7 Stacked tetrakaidecahedron cells: (a) Three-dimensional view,
(Gibson and Ashby, 1997)



(b)

Figure 2 7 (Continued): (b) Two-dimensional views.

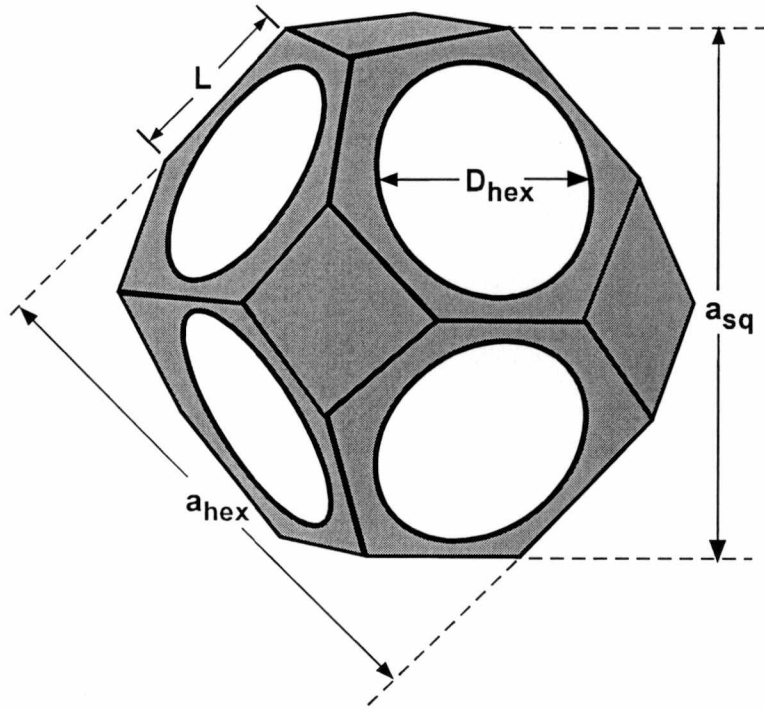


Figure 2.8: Tetrakaidecahedron unit cell.

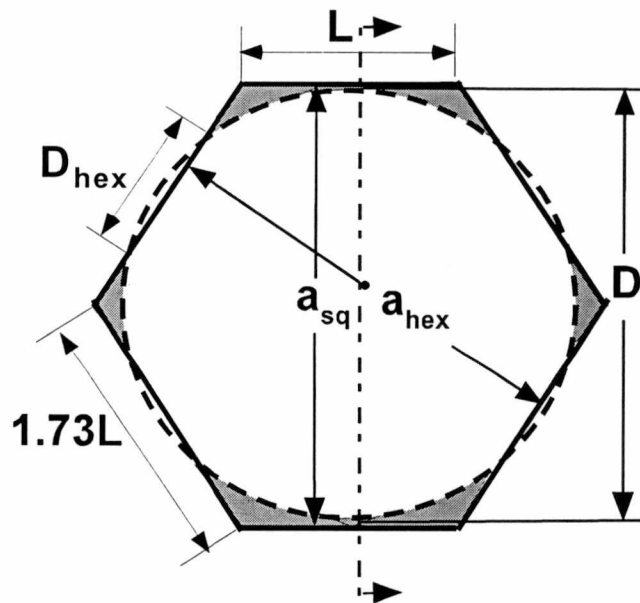


Figure 2.9: Two-dimensional projection of the mid-plane of the unit cell.

As it can be indicated in Figure 2.9, the distance between any two mutually parallel *sides* of the hexagonal face is $1.73L$ ($\sqrt{3}L$). The distance between any two mutually parallel *square faces*, a_{sq} , can be expressed in term of the edge length, L , by

$$a_{sq} = 2.83L \quad (2.30)$$

whereas the distance between two mutually parallel hexagonal faces, a_{hex} , is given by

$$a_{hex} = 2.45L \quad (2.31)$$

The diameters of the circles on the hexagonal face, D_{hex} , can be related to D and a_{hex} , by using the Pythagorean theorem:

$$D_{hex} = 2 \left[\sqrt{\left(\frac{D}{2}\right)^2 - \left(\frac{2.45L}{2}\right)^2} \right] \quad (2.32)$$

The void volume in the cell, V_{void} , is equal to the volume of the sphere subtracting the eight spherical end caps on the hexagonal faces, V_{ch} , that is

$$V_{void} = \frac{\pi D^3}{6} - 8V_{ch} \quad (2.33)$$

where

$$V_{ch} = \frac{\pi}{12} (D - 2.45L)^2 \left(D + \frac{2.45L}{2} \right) \quad (2.34)$$

The volume of the tetrakaidecahedron unit cell is given by (Gibson and Ashby, 1997):

$$V_{cell} = 11.31L^3 \quad (2.35)$$

Thus, the foam porosity, ϕ , is related to L and the pore size D by

$$\phi = \frac{\left[\frac{\pi D^3}{6} - 8 \left\{ \frac{\pi}{12} (D - 2.45L)^2 \left(D + \frac{2.45L}{2} \right) \right\} \right]}{11.31L^3} \quad (2.36)$$

The surface area of the tetrakaidecahedron cell contacting with the fluid, A_{cell} , is equal to the surface area of the sphere, A_s , subtracting the areas of the eight spherical end caps on the hexagonal faces, A_{ch} , i.e.:

$$A_s = \pi D^2 \quad (2.37a)$$

$$A_{cell} = A_s - 8A_{ch} \quad (2.37b)$$

where

$$A_{ch} = \pi \left\{ \left(\frac{D}{2} - \frac{2.45L}{2} \right)^2 + 2 \left(\frac{D_{hex}}{2} \right)^2 \right\} \quad (2.38)$$

Therefore, the surface area density of the foam, α_A , defined as the surface area per unit volume of the unit cell is given by

$$\alpha_A = \frac{\pi D^2 - 8\pi \left\{ \left(\frac{D}{2} - \frac{2.45L}{2} \right)^2 + 2 \left(\sqrt{\left(\frac{D}{2} \right)^2 - \left(\frac{2.45L}{2} \right)^2} \right)^2 \right\}}{11.31L^3} \quad (2.39)$$

It is noted that Eq. (2.39) represents an estimate of the average surface area density of the graphite foam in terms of mean pore size and mean size of the cell when using the tetrakaidecahedron cell model

2.2.2 Fluid velocity profile

The fluid flow in porous media is a rather complex phenomenon and despite the computational resources we have nowadays, the analysis of fluid flow in porous medium still relies heavily on observation and measurement of actual flow patterns. The principle of dynamical similarity and the use of dimensionless parameters provide us with a very useful technique to translate measured results from one flow configuration to

another

One important dimensionless parameter is the Reynolds number, which is defined by

$$\text{Re}_{\max} = \frac{u_{\max} D_h}{\nu_f} \quad (2.40)$$

where u_{\max} is the maximum velocity of the fluid passing through the foam, ν_f is the fluid kinematic viscosity, and D_h is the hydraulic diameter for the graphite foam, which is defined as four times the flow area per wetted perimeter for flows through a non-circular cross-sectional pipe (Rohsenow *et al*, 1985). The difference between Eq. (2.40) and Eq. (1.5), which was used to define the Reynolds number for flow past a heated single cylinder or a bank of heated cylinders, is the replacement of the cylinder diameter, d , by the hydraulic diameter D_h , a commonly used characteristic length for porous media. This is based on the point of view that a porous medium may be viewed as an aggregation of flow passages rather than as an aggregation of solid bodies (Tong and London, 1957). It can be readily shown that Eq. (2.40) coincides with the usual one when considering flow in cylindrical passages.

According to Carman-Kozeny theory (Dullien, 1992), which is based on a semiheuristic model of flow through solid matrices, the hydraulic diameter, D_h , is defined as four times the void volume per surface area.

$$D_h = \frac{4V_{void}}{A_{cell}} = \frac{4\phi}{\alpha_A} \quad (2.41)$$

where V_{void} is the unit void volume and A_{cell} is the internal surface area of a unit cell. For example, the hydraulic diameter for crossed-rod and woven-screen matrices can be expressed by (Coppage and London, 1956)

$$D_h = \frac{4L_p A_c}{A_{total}} \quad (2.42)$$

where A_{total} is the total surface area of the matrix, A_c is the minimum free flow cross-sectional area, and L_p is the total length of the core structure in the flow direction.

In order to establish the velocity profile for the fluid passing through the graphite foam, the Reynolds number, Re_{max} , based on the maximum velocity within the foam, u_{max} , is used. From the conservation of mass, u_{max} , occurring in the minimum flow area A_c is given by

$$u_{max} = \frac{A_{fr}}{A_c} u_{avg} = \frac{2.598L^2}{\pi \left(\left(\frac{D}{2} \right)^2 - \left(\frac{2.45L}{2} \right)^2 \right)} u_{avg} \quad (2.43)$$

where u_{avg} is the average free stream velocity, the (frontal) area of the hexagonal surface, A_{fr} , is given by

$$A_{fr} = 6 \left(\frac{\sqrt{3}}{4} \right) L^2 \approx 2.598L^2 \quad (2.44)$$

and the minimum flow area A_c is given by

$$A_c = \frac{\pi}{4} D_{hex}^2 \quad (2.45)$$

2.2.3 Fluid temperature profile

The temperature of the cooling fluid increases continuously as it flows along the passages provided by the pores within the graphite foam, as the driving force for heat transfer continuously diminishes. Because it is very difficult to determine the detailed temperature profile of the fluid everywhere in the passages, the mean bulk temperature of the cooling fluid, T_b , given by

$$T_b = T_1 - \Delta T_m \quad (2.46)$$

is used, where T_1 is the constant temperature of the top surface of the foam, and ΔT_m is the well-known logarithmic mean temperature difference defined by Eq (2.28).

It is assumed that the turbulent flow inside the foam is well mixed and the heat transfer between the cooling fluid and the graphite foam is characterized by the convective heat transfer coefficient, h , which depends on:

- The viscosity, μ_f , of the cooling fluid,
- The specific heat, c_p , of the cooling fluid;
- The density, ρ_f , of the cooling fluid;
- The size of the graphite foam specified by some characteristic dimension, D_h ;
- The magnitude of the forced cooling fluid velocity as specified by the maximum velocity of the fluid, u_{max} , as it passes through the graphite foam;

All of the properties of the cooling fluid are evaluated at its mean bulk temperature, T_b

2.2.4 Pressure drop

The foam immersed in a fluid experiences forces due to the interaction between the foam and the fluid passing through it. The forces at the fluid and foam interface can be described in terms of the wall shear stresses, τ_w , due to viscous effects, and the normal stresses (pressure), p_w . Friction factor is in general defined as the equivalent shear force in the flow direction per unit of heat transfer or friction area, thus the relationship between friction factor, f , and the Reynolds number based on the maximum fluid velocity, Re_{max} , is generally given in the form of (Kays and London, 1984)

$$f = B Re_{max}^{-m} \quad (2.47)$$

where B and m are constants.

For graphite foams, the pressure drop across the foam can be expressed by (Tee, 2000)

$$\Delta p = \frac{\rho_f u_{\max}^2}{2} \left[f \frac{4L_p}{D_h} \right] \quad (2.48)$$

Substitution of Eq (2.40), (2.41), and (2.47) into Eq. (2.48) gives

$$\frac{\Delta p}{L_p} = \frac{2^{-2m-1} B \rho_f \nu_f^m}{\phi^{1+m}} \left(\frac{2.598 L^2}{\pi \left(\left(\frac{D}{2} \right)^2 - \left(\frac{2.45L}{2} \right)^2 \right)} u_{avg} \right)^{2-m} \left(\frac{\pi D^2 - 8\pi \left\{ \left(\frac{D}{2} - \frac{2.45L}{2} \right)^2 + 2 \left(\sqrt{\left(\frac{D}{2} \right)^2 - \left(\frac{2.45L}{2} \right)^2} \right)^2 \right\}}{11.31 L^3} \right)^{1+m} \quad (2.49)$$

By inputting the fluid physical properties ρ_f and ν_f , the velocity of the free stream flow u_{avg} the porosity of the graphite foam ϕ , the mean pore diameter of the spherical void D , the unit cell edge length L , which can be determined from Eq (2.36), the coefficient B , and the exponent m in the power law relationship of the experimental friction data, the pressure drop across the graphite foam based on the tetrakaidecahedron cell model can be estimated by Eq. (2.49).

Unfortunately, the coefficient and exponent in Eq. (2.47) for graphite foam are not available at this moment. Thus, the data for woven-screen matrices ($B = 23.9$, and $m = 0.7$) are used to model the frictional characteristics of graphite foam. The pressure

drop per unit length, $\Delta p / L_p$, as a function of average free stream velocity, u_{avg} , for air at 20 °C ($\nu_f = 1.46 \times 10^{-5} \text{ m}^2/\text{s}$ and $\rho_f = 1.23 \text{ kg/m}^3$) flowing through a duct filled with graphite foam ($D = 300 \text{ }\mu\text{m}$ and $\phi = 80\%$) is shown in Figure 2.10a. The experimental pressure drop data for Mitsubishi ARA24 mesophase pitch derived graphite foam (Klett, 1999a) is also shown in Figure 2.10a. It can be seen that the model agrees well with the experimental data. The final expression of the pressure drop prediction of the ARA24 foam can be written by

$$\frac{\Delta p}{L_p} = \frac{4.53 \rho_f \nu_f^m}{\phi^{1+m}} \left(\frac{2.598 L^2}{\pi \left(\left(\frac{D}{2} \right)^2 - \left(\frac{2.45L}{2} \right)^2 \right)} u_{avg} \right)^{1.3} \left\{ \frac{\pi D^2 - 8\pi \left\{ \left(\frac{D}{2} - \frac{2.45L}{2} \right)^2 + 2 \left(\sqrt{\left(\frac{D}{2} \right)^2 - \left(\frac{2.45L}{2} \right)^2} \right)^2 \right\}}{11.31 L^3} \right\}^{1.7} \quad (2.50)$$

The pressure drop for water (20°C) with $c_p = 4.182 \text{ KJ/Kg-}^\circ\text{C}$, $\nu_f = 1.004 \text{E-6 m}^2/\text{s}$, $\text{Pr} = 6.99$, and $\rho_f = 998.3 \text{ Kg/m}^3$ passing through the same foam is shown in Figure 2.10b.

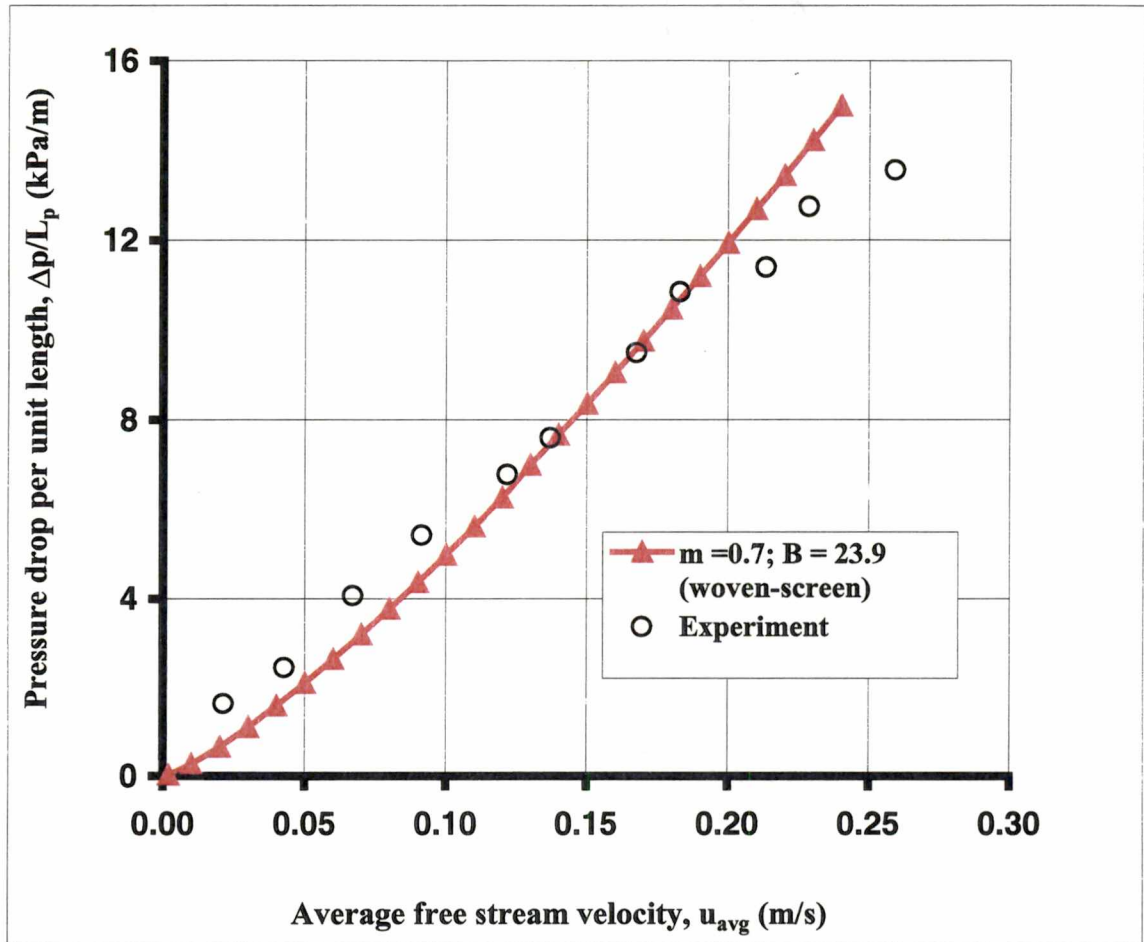


Figure 2.10: Pressure drop per unit length, $\Delta p/L_p$, across graphite foam ($D = 300\mu\text{m}$; $\phi = 80\%$) as a function of fluid velocity, u_{avg} , for (a) air (20°C) and (b) water (20°C) by using the friction data for woven-screen matrices.

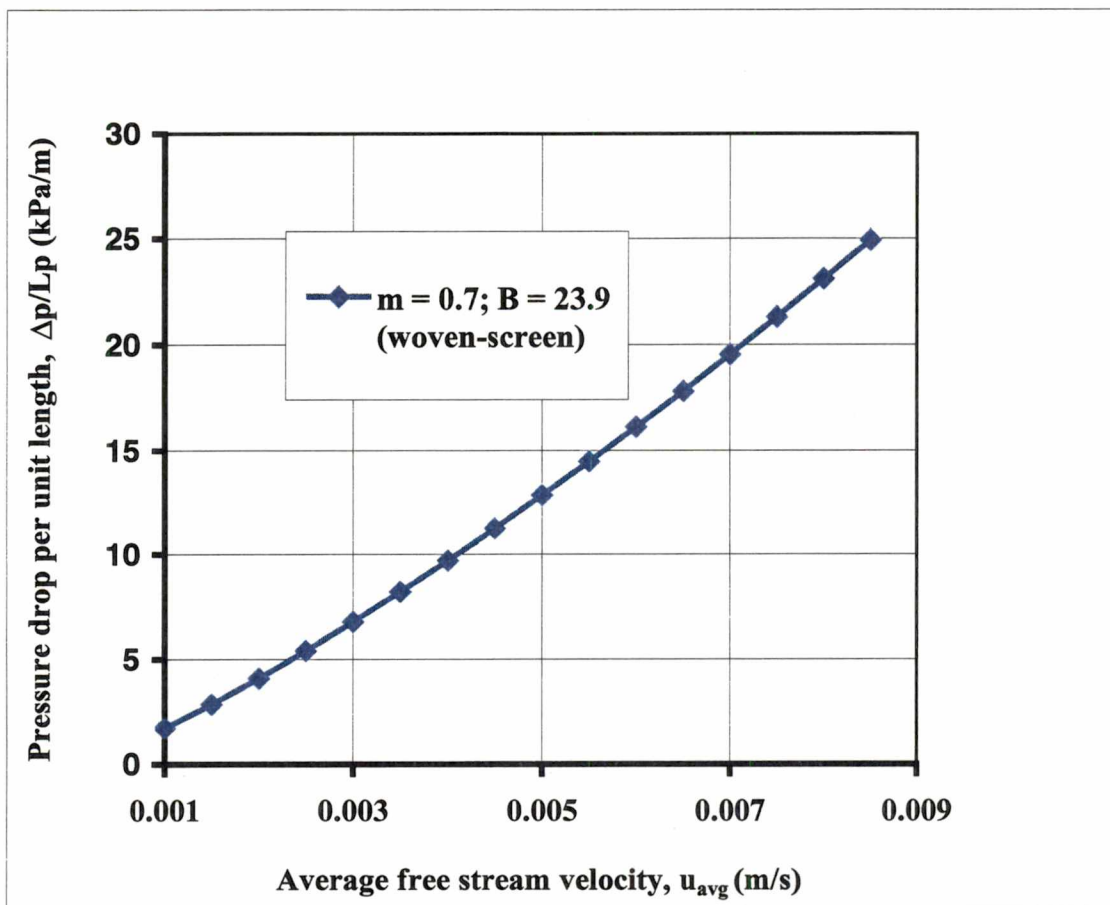


Figure 2.10 (Continued): (b) Water

2.2.5 Overall convective heat transfer coefficient

The transfer of energy due to a low-density streaming flow past a heated matrix having large surface area density is a subject of enormous studies, but the existing results are largely limited to empirical corrections. For most of the practical applications, the heat convection for different fluid/solid contacting surfaces can be expressed in the following form (Kays and London, 1984)

$$St Pr^{2/3} = \Phi(Re) \quad (2.51)$$

where, $\Phi(Re)$ is a functional of Reynolds number and the Stanton number is defined by

$$St = \frac{Nu}{Re_{\max} Pr} = \frac{h_{\text{overall}}}{\rho_f c_p u_{\max}} \quad (2.52)$$

The Prandtl number is not a test variable. The two-thirds power of the Prandtl number in Eq. (2.51) is adequate for gases with Prandtl numbers ranging from 0.5 to 15 (Kays and London, 1984). For turbulent flows in tubes, the available analytic solutions suggest that $(Pr)^{1/2}$ should be used in Eq. (2.51), but the two-thirds power is still a reasonable approximation (Kays and London, 1984).

In the previous subsection, one finds that the tetrakaidecahedron cell model using the friction parameters of woven-screen matrixes ($B = 23.9$; $m = 0.7$) agrees well with the experimental data obtained for graphite foam. Therefore, it is further assumed that

the heat transfer in graphite foam is also very similar to that in the woven-screen matrices. According to Tong and London (1956), Eq. (2.51) becomes

$$StPr^{2/3} = 0.375Re'^{-0.375} \quad (2.53)$$

for woven-screen matrices, where Re' is a "modified" Reynolds number given by

$$Re' = \frac{1 - F\phi}{F\phi} Re_{\max} \quad (2.54)$$

where

$$F = 0.96 \quad \text{for } Re' > 1800 \quad (2.55a)$$

$$F = 1.155 - 0.0601 \log_{10} Re' \quad \text{for } Re' < 1800 \quad (2.55b)$$

and ϕ is the porosity of the matrix. For graphite foam, in most conditions Re' is usually less than 100–200. To facilitate the use of Eq. (2.53), Fig. 2.11 is prepared, giving $Re'/Re_{\max} = (1 - F\phi)/F\phi$ as a function of Re_{\max} . Substitution of Eq. (2.52) into Eq. (2.53) gives

$$h_{\text{overall}} = 0.375 Pr^{-2/3} Re'^{-0.375} c_p \rho_f u_{\max} \quad (2.56)$$

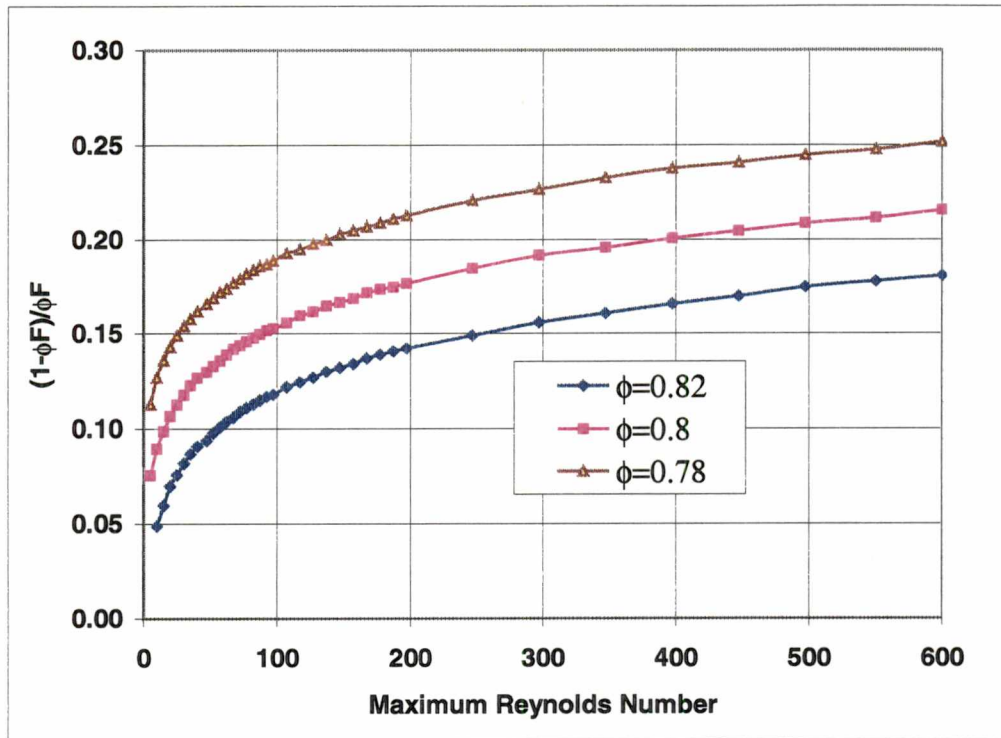


Figure 2.11: $Re'/Re = (1-F\phi)/F\phi$ versus Re_{max} for graphite foam ($D=300\mu m$) with porosity $\phi=78\%$, 80% , and 82% .

With the aid of Eq (2.40) and (2.54), Eq. (2.56) is rewritten to give the overall convective heat transfer coefficient of the graphite foam

$$h_{overall} = 0.375 \text{Pr}^{-2/3} \left(\frac{1 - F\phi}{F\phi} \right)^{-0.375} \left(\frac{u_{max} D_h}{\nu_f} \right)^{-0.375} c_p \rho_f u_{max} \quad (2.57)$$

where u_{max} and D_h are given in Eq (2.43) and (2.41), respectively. Thus by inputting the fluid physical properties ρ_f , c_p , and ν_f , the velocity of the free stream flow u_{avg} , the porosity of the graphite foam ϕ , the mean diameter of the spherical void D , the unit cell edge length L , which can be determined from Eq. (2.36), and the surface area density α_A , which can be obtained from Eq (2.39), the overall convective heat transfer coefficient of the graphite foam based on the tetrakaidecahedron cell model is estimated by Eq (2.57)

2.2.6 Results and discussion

Thermal testing is carried out using four graphite foam blocks in the same heat exchanger test chamber (Tee, 2000). The experimental configuration, which is shown in Fig 2.12, is composed of an aluminum plate and a graphite foam block encapsulated within a nylon test chamber used to provide the thermal insulation. The graphite foam block is attached to an aluminum base by brazing with Superbraz[®], a high thermal conductivity braze manufactured by Materials Resources International, Inc. Two cartridge heaters are used to create isothermal heating and are mounted on the top of the

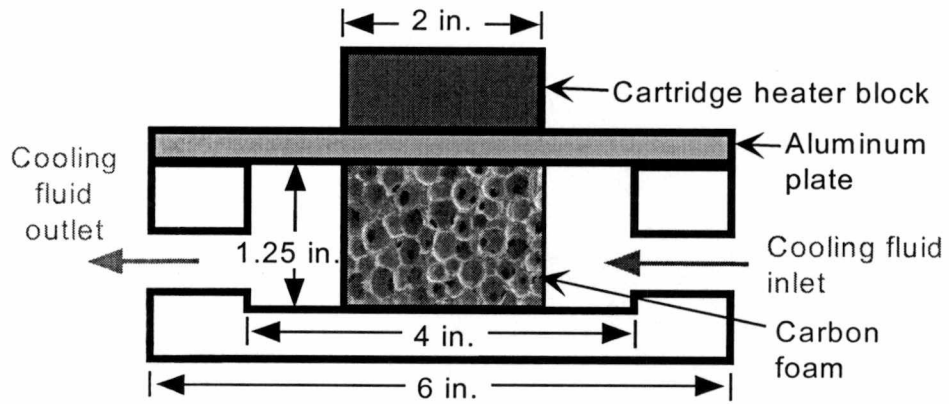


Figure 2.12: Experimental configuration of the heat exchanger system (Tee, 2000).

aluminum plate Air at lower temperature is forced to pass through the graphite foam at flow rates from 140 to 400 liter/minute. Four thermocouples are arranged to measure the inlet and outlet air temperature, and the temperature of the aluminum plate and the cartridge heater The samples used, which are fabricated at different processing conditions, foam densities, and geometrical designs, are labeled as 1 to 4 with all of the detailed dimensions and foam densities being listed in Table 2.1.

In comparison with the cubic model presented in subsection 2.1, the tetrakaidecahedron model agrees much better with the data obtained from the experiments (Tee, 2000) Figures 2.13 to 2.15 show how the variation of pore diameter D , porosity of graphite foam, ϕ , and free stream velocity u_{\max} of air (20°C) affects the

Table 2 1: Dimensions and densities of the graphite foam blocks tested in the heat exchanger chamber (Tee, 2000).

Graphite Foam Block	Density (g/cm ³)	Height cm (inch)	Length cm (inch)	Width cm (inch)
Sample #1	0.43	3.16 (1.24)	5.04 (1.99)	5.12 (1.98)
Sample #2	0.47	3.20 (1.26)	5.14 (2.02)	5.07 (2.00)
Sample #3	0.48	3.17 (1.25)	5.24 (2.06)	5.05 (1.99)
Sample #4	0.46	3.21 (1.26)	5.21 (2.05)	5.04 (1.98)

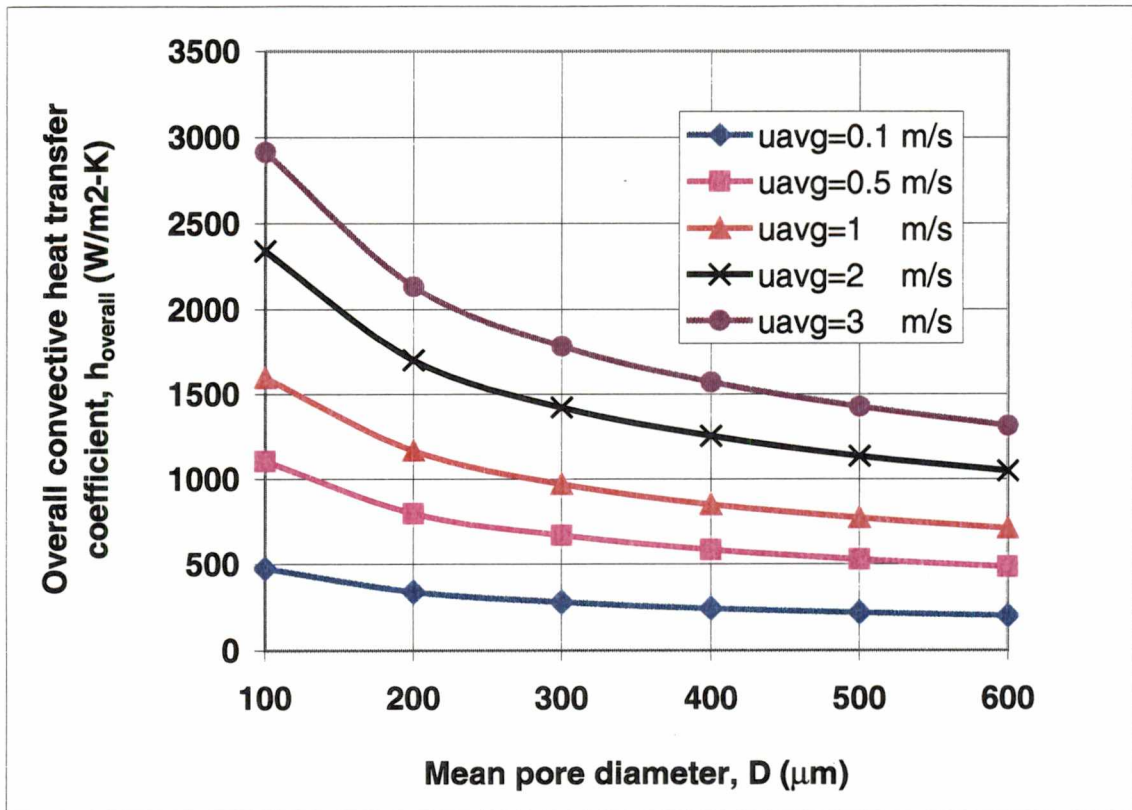


Figure 2.13: Overall convective heat transfer coefficient as a function of mean pore diameter, D , of graphite foam with a porosity of 80%, for air (20°C) with different velocities.

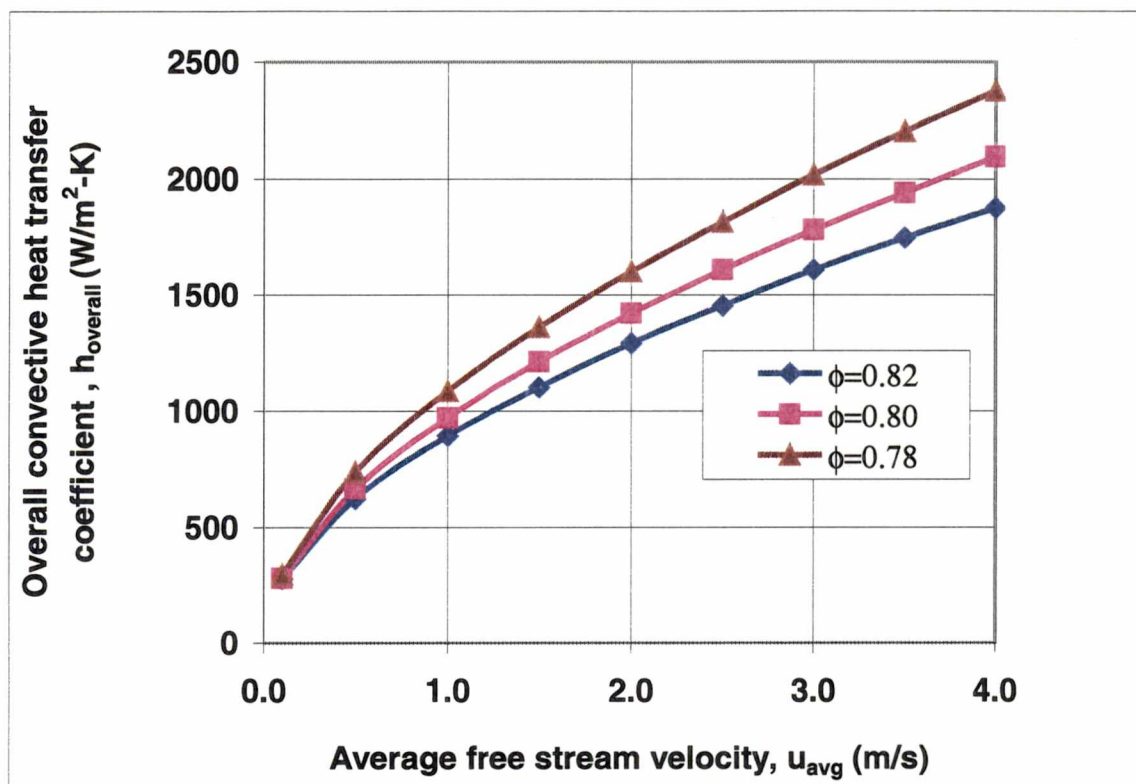


Figure 2.14: Overall convective heat transfer coefficient of graphite foams with mean pore diameter, $D=300\mu\text{m}$ and porosities of 78%, 80%, and 82% as a function of average free stream velocity, u_{avg} , for air (20°C).

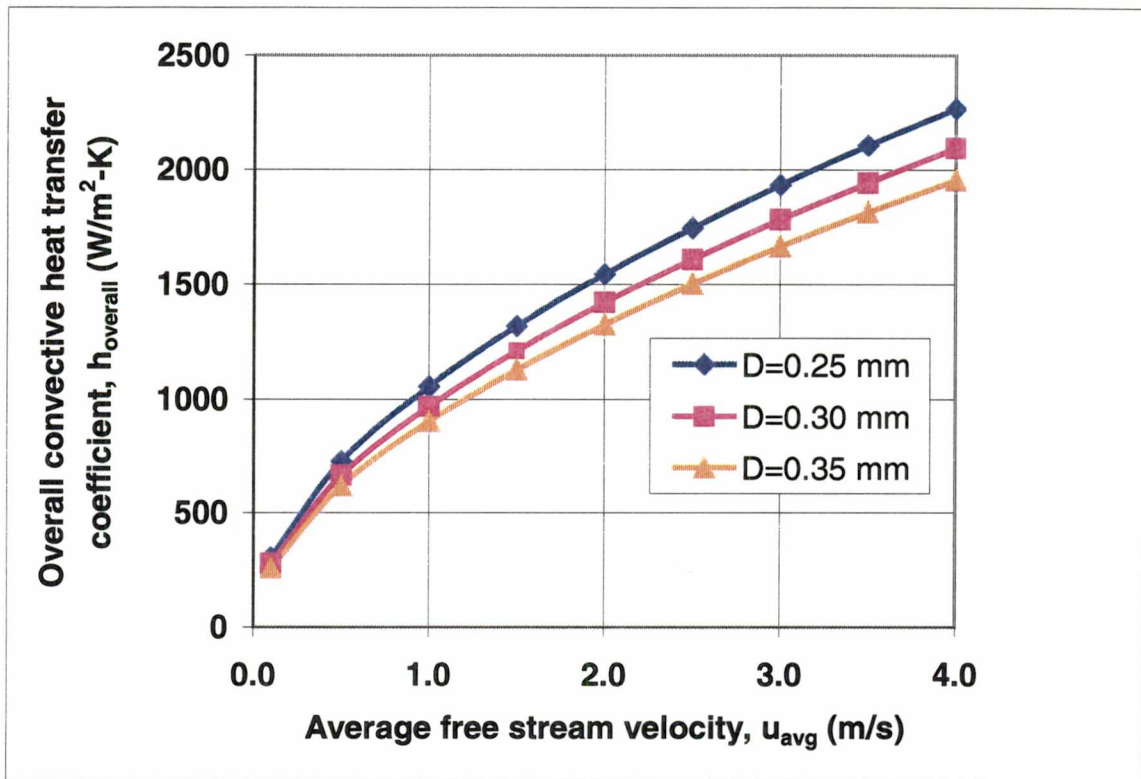


Figure 2.15: Overall convective heat transfer coefficient of graphite foams with mean pore diameter, $D= 250\mu\text{m}$, $300\mu\text{m}$, and $350\mu\text{m}$, and porosity of 80% as a function of average free stream velocity, u_{avg} , for air (20°C).

overall convective heat (transfer coefficient, $h_{overall}$. For air at 20°C, $c_p = 1\,006$ KJ/Kg-°C, $\nu_f = 15\,09E-6$ m²/s, Pr =0.71, and $\rho_f = 1.2042$ Kg/m³. It is noted that the overall heat transfer coefficient, $h_{overall}$, increases with an increase in the average velocity of the cooling fluid. The overall heat transfer coefficient, $h_{overall}$, however decreases with an increase in the porosity of the foam, ϕ , an increase in the mean pore diameter, D , or both due to the decrease in surface area density α_A . Figure 2.16 indicates that the mean bulk temperature of the air does not have a significant effect on the overall heat transfer coefficient of graphite foams

As it is indicated in Figure 2.17, the difference between the convective heat transfer coefficients predicted by the tetrakaidecahedron cell model using the friction parameter of woven-screen matrices and those determined experimentally ranges from 1% (sample #2) to 65% (sample #3). It is noted that the experimental data might contain errors due to the variance in ambient air inlet temperature, humidity, or uncertainty in the experimental setup. Figure. 2 17 shows that sample #2 and #3, which have the same processing condition and approximately the same density, exhibit very different convective heat transfer coefficients obtained by experiments. Therefore an error within the range of 100% is not unreasonable (Lu *et al* , 1998). One thus concludes that the tetrakaidecahedron cell model is reasonably acceptable for predicting the heat transfer in graphite foam. However, more experiments should be conducted to draw a better conclusion about the present model's predictions. Figure 2 18 to 2 21 discuss the same effects on $h_{overall}$ by considering water as the cooling fluid.

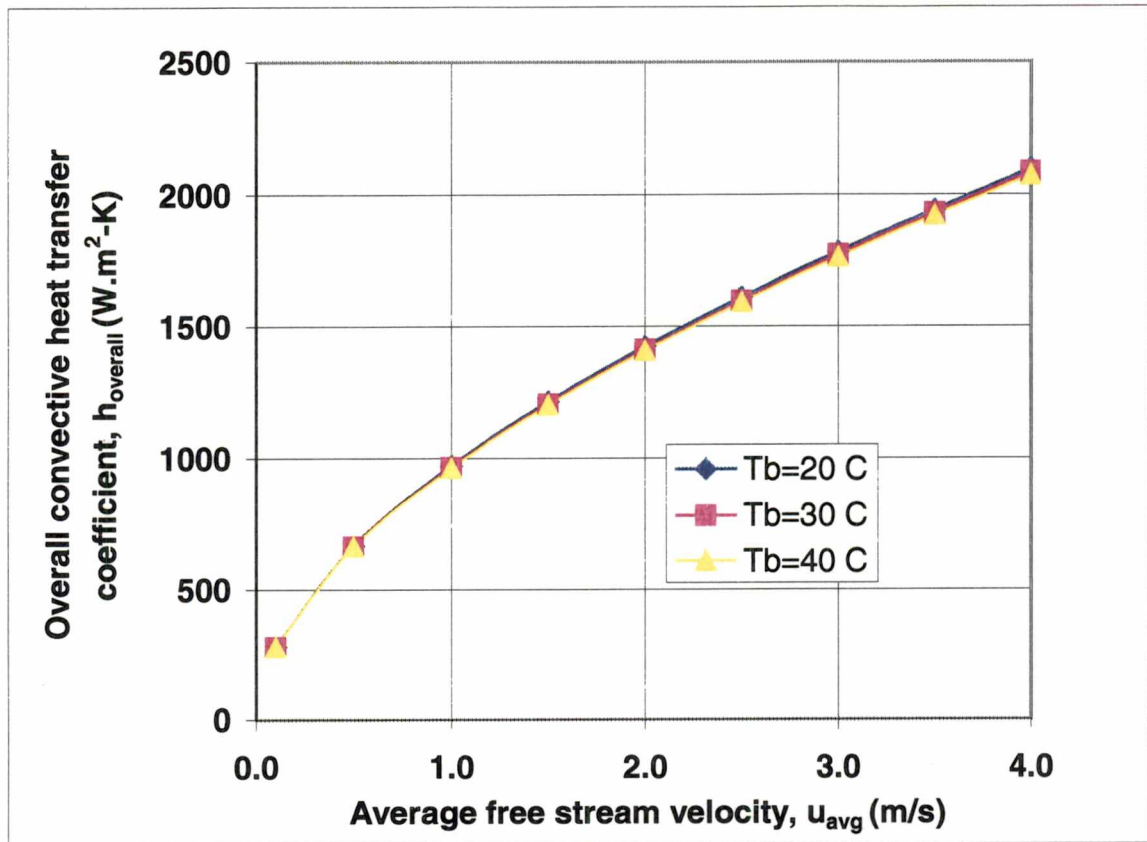


Figure 2.16: Overall convective heat transfer coefficient of graphite foam with porosity of 80%, and a mean pore diameter, $D=300\mu\text{m}$ as a function of average free stream velocity, u_{avg} , for air with different mean bulk temperature.

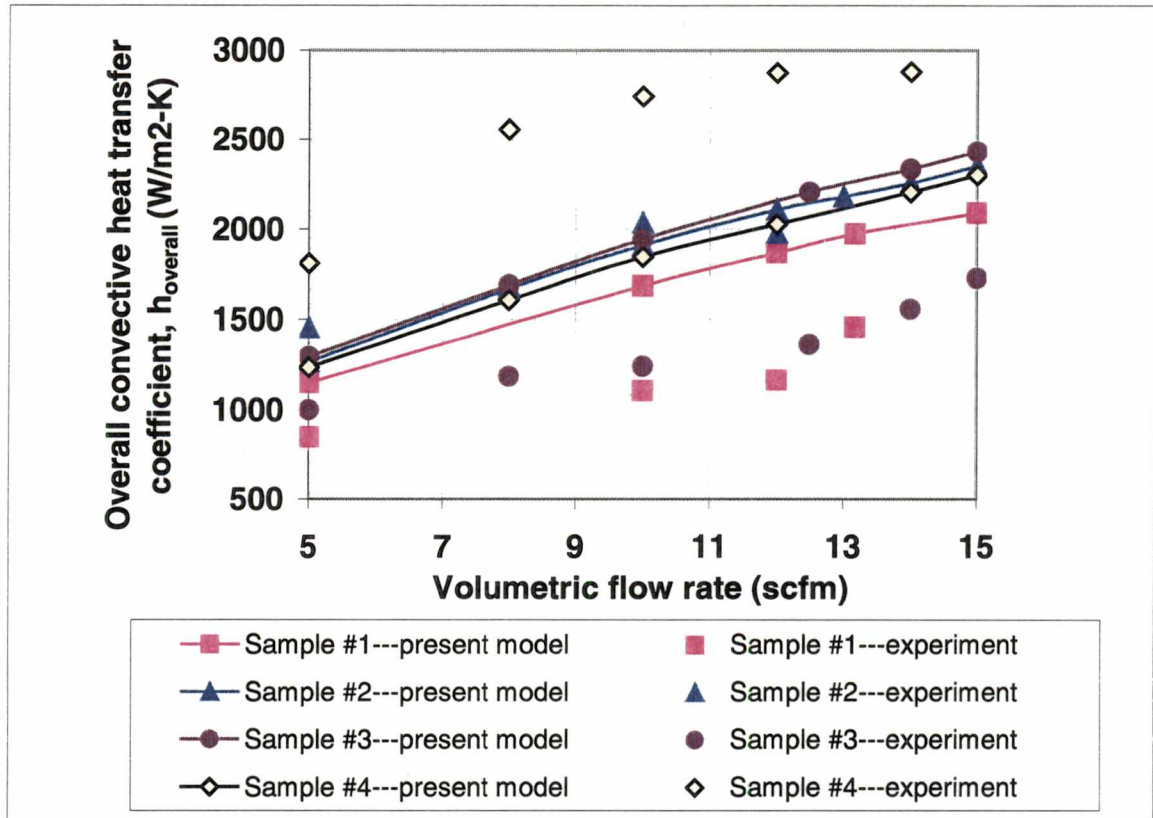


Figure 2.17: Overall convective heat transfer coefficient as a function of flow rate for heat exchangers using graphite foams.

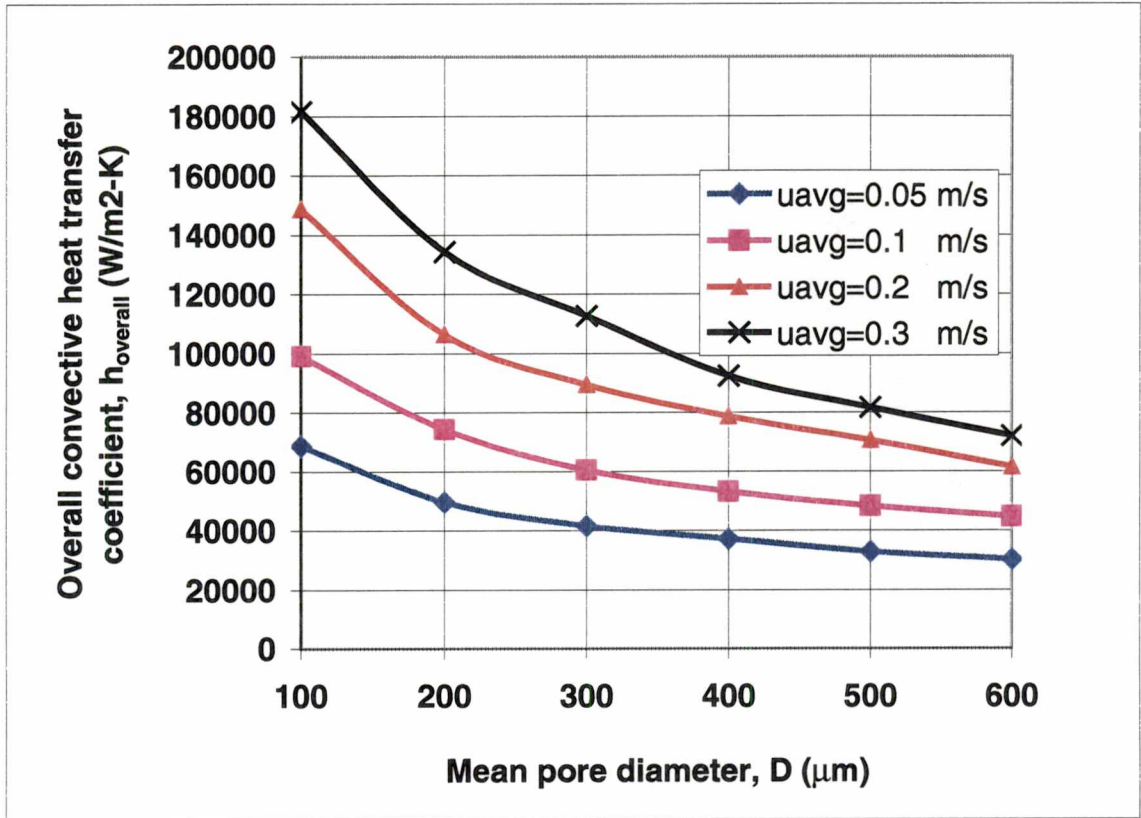


Figure 2.18: Overall convective heat transfer coefficient as a function of mean pore diameter, D , of graphite foam with a porosity of 80%, for water (20°C) with different velocities.

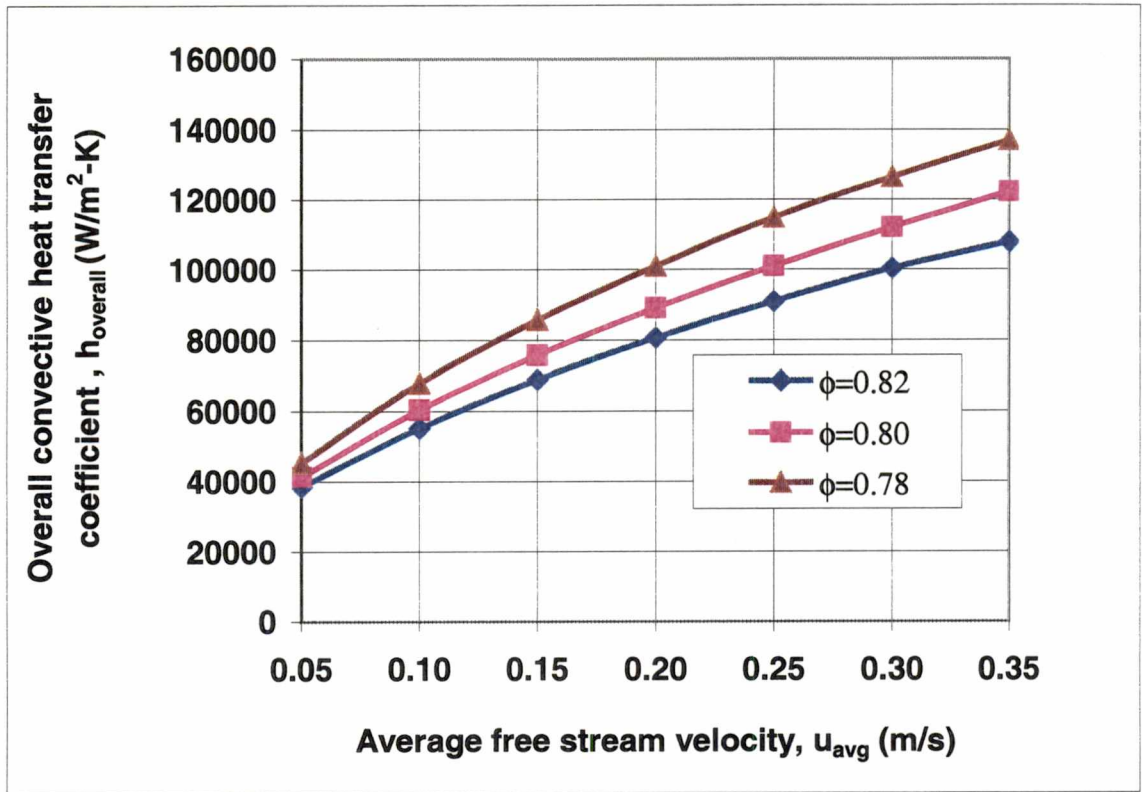


Figure 2.19: Overall convective heat transfer coefficient of graphite foams with mean pore diameter, $D=300\mu m$ and porosities of 78%, 80%, and 82% as a function of average free stream velocity, u_{avg} , for water ($20^{\circ}C$).

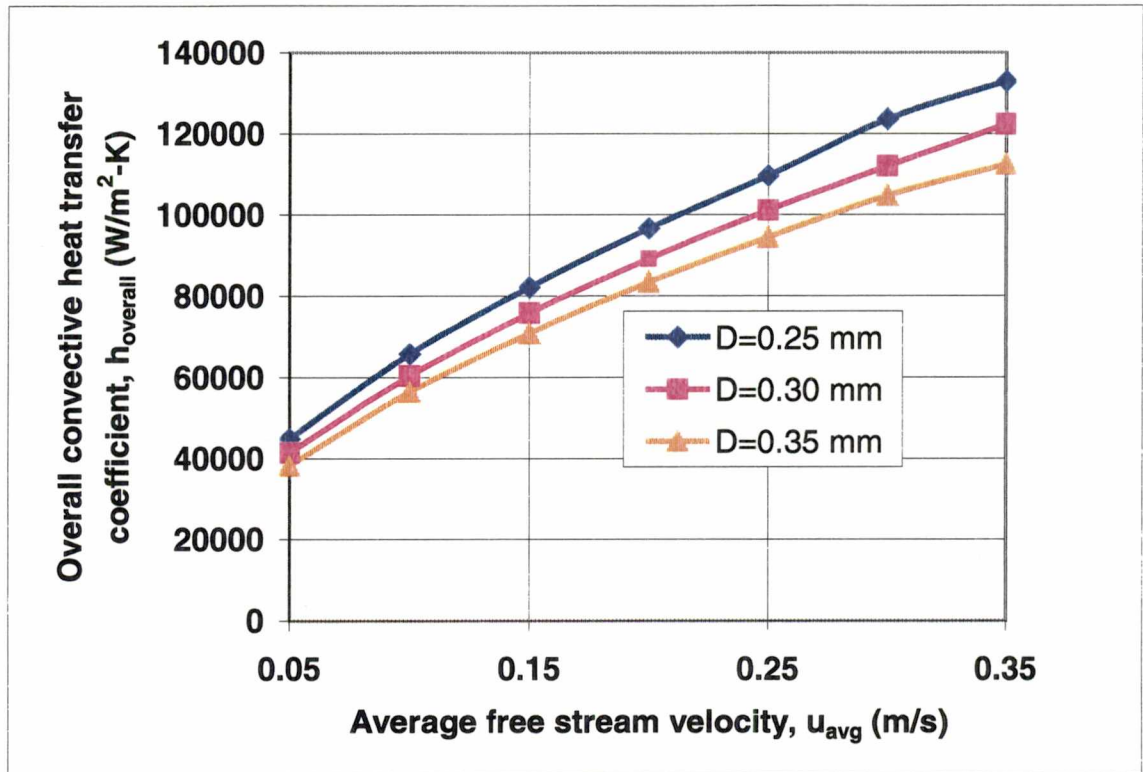


Figure 2.20: Overall convective heat transfer coefficient of graphite foams with mean pore diameter, $D= 250\mu\text{m}$, $300\mu\text{m}$, and $350\mu\text{m}$, and porosity of 80% as a function of average free stream velocity, u_{avg} , for water (20°C).

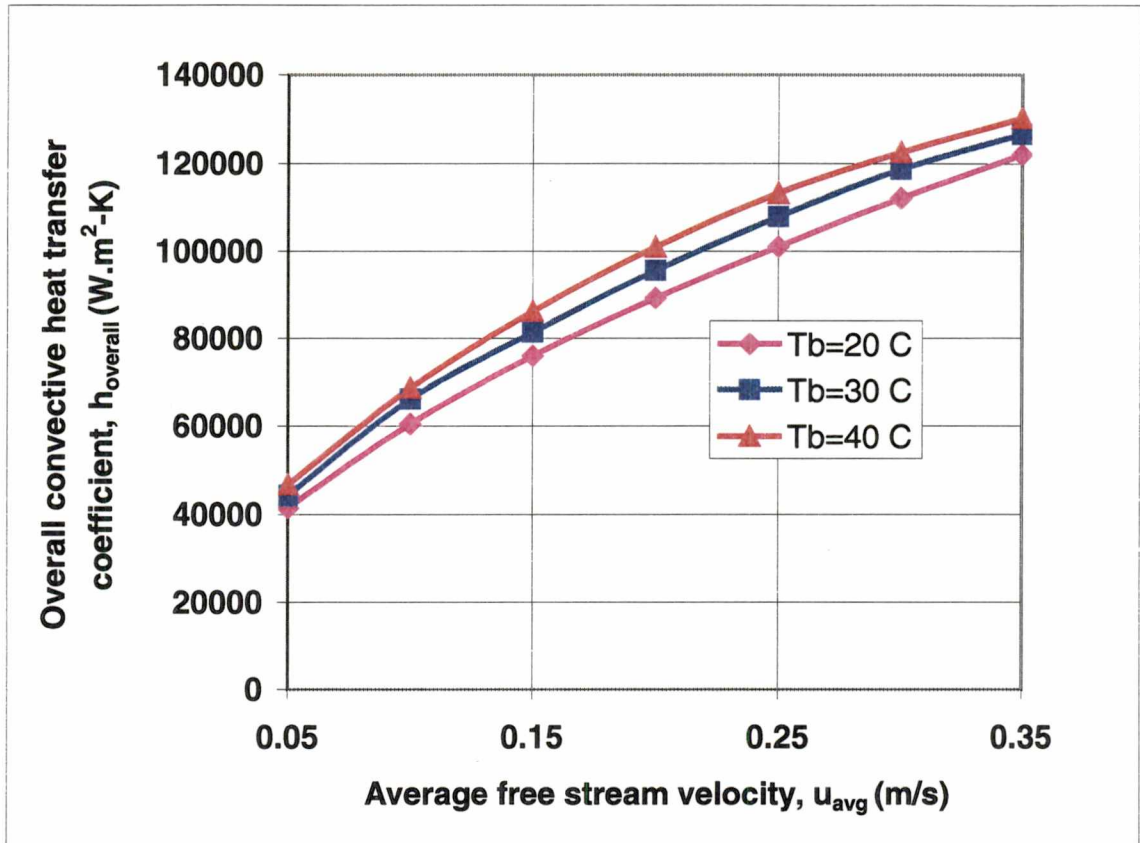


Figure 2.21: Overall convective heat transfer coefficient of graphite foam with porosity of 80%, and a mean pore diameter, $D=300\mu\text{m}$ as a function of average free stream velocity, u_{avg} , for water with different mean bulk temperature.

CHAPTER 3

CONCLUSIONS AND DISCUSSIONS

ON GRAPHITE FOAM

The interaction between the pressure drop and the forced heat convection in the mesophase pitch-derived graphite foam is of interest in order to optimize the performance of heat exchanger using graphite foam as the core material. The analytical modeling on overall convective heat transfer coefficient as well as pressure drop of the graphite foams is reported in the present work. It is noted that the merit of graphite foam such as lightweight, isotropic thermal conductivity, acceptable mechanical properties, and the continuous, open-cell graphitic networks may lead to novel and interesting applications of thermal management

While both the cubic cell model and the tetrakaidecahedron cell model show that overall convective heat transfer coefficient increases with an increase in free-stream velocity and a decrease in cell size, which is in agreement with the experiments data obtained by Tee (2000) However, the predicted values of $h_{overall}$ by the cubic cell model are much higher than those predicted by the tetrakaidecahedron cell model, which fall within the wide range of experimental data. The reason is probably because the tetrakaidecahedron cell model, resembling the shape of a sphere, is a better geometric representative of the mesophase pitch-derived graphite foam. In particular, the surface area density of the graphite foam can be accurately determined with the aid of the tetrakaidecahedron model, which may be critical in estimating the pressure drop as well

as the heat transfer coefficient of porous foam (Gibson and Ashby, 1997) In addition, the velocity profile and the temperature distribution of the fluid flowing through the graphite foam are strongly dependent on the foam morphology. Therefore, the judicious selection of the representative cell becomes crucial. Another important reason may be because that the graphite foam should be regarded as an aggregation of passages rather than struts (Kays and London, 1984) It is noted that the tetrakaidecahedron cell model, based on the view promoted by Tong and London (1957) that a porous medium may be viewed as an aggregation of flow passages, doesn't explicitly include the conductivity of the foam in formulating the overall convective heat transfer coefficient, $h_{overall}$ But it doesn't mean that the conductivity of the foam has no effects on the heat transfer in graphite foam. The high convective heat transfer coefficient together with high thermal conductivity is closely related to pressure drop and overall heat transfer coefficient of graphite foam

Generally, the design of a heat exchanger involves the consideration of both the heat transfer rates and the mechanical pumping power expended to overcome fluid friction and to move the fluid through the heat exchanger For gas-flow heat exchangers, the friction-power limitations generally force a design for moderately low mass velocities of fluid as a high fluid-flow velocity results in the increase in the friction-power expenditure Therefore, low mass velocities of fluid, together with the low thermal conductivities of the gases (relative to liquids), result in low heat transfer rates per unit surface area in conventional heat exchangers. Thus a large amount of surface areas become a typical characteristic of gas-flow heat exchangers. One of the advantages

of graphite foams is that they can provide flow passages with very large surface area densities. But the increase in surface area density in turn increases the friction-power expenditure. In a heat exchanger system, the heat transfer rate, q , and pressure drop (or, equivalently, pumping power), Δp , often have the following approximate proportionality with fluid velocity, u (Bell, 1990)

$$\Delta p \propto u^\lambda \quad (3.1)$$

$$q \propto u^j \quad (3.2)$$

where λ ranges from 1.0 to 1.8 and j ranges from 0.3 to 0.6 for a typical heat exchanger. From Eq (2.50) and Eq (2.57), one finds that for graphite foam, the following relationships hold.

$$\Delta p \propto u^{1.3} \quad (3.3)$$

$$q \propto u^{0.625} \quad (3.4)$$

Therefore, optimizing the performance of foam as a core material for heat exchangers is essentially the optimization of heat transfer rate while maintaining relatively low pressure drop across the foam. The tetrakaidecahedron cell model can be a valuable tool for designing foam structures resulting in optimal heat transfer per unit pumping power.

Based on the experimental results by Tee (2000), the overall heat transfer coefficient of heat exchanger using graphite foam core is approximately $3,000 \text{ W/m}^2\text{K}$, which is significantly higher than that of a standard automobile radiator of $30 \text{ W/m}^2\text{K}$. In order to optimize the heat exchanger behavior of graphite foams, additional thermal testing with different heat exchanger designs utilizing graphite foams as the core materials is recommended for a better understanding of the performance of graphite foams

CHAPTER 4

INTRODUCTION ON FIBER-REINFORCED COMPOSITES

The finite element method (FEM) is employed to compute the longitudinal Young's modulus of a single short fiber-reinforced composite subjected to uniaxial tension. Effects of microstructural parameters such as fiber aspect ratio are studied and the finite element analysis (FEA) results are compared with those obtained from the modified shear lag model (Hsueh, 2000).

4.1 Background

4.1.1 *Composite materials*

A composite material is defined as a heterogeneous material having chemically and/or physically distinct phases (reinforcements) distributed within a continuous phase (matrix). It is only when the constituents have significantly different physical/chemical properties and thus the composite properties are noticeably different from the constituent properties that the heterogeneous materials can be recognized as composites (Agarwal *et al*, 1990). While the matrix phase is the continuous phase, the distributed phase(s) can be in the form of particles, whiskers, short fibers, continuous fibers, laminae, or the combination of any of them. Generally, the composite materials are divided into four categories: fibrous, particulate, laminated, and hybrid composites (Richardson, 1987). Based on the material characteristics of matrix, the composite materials may be

classified as ceramic matrix composites (CMCs), metal matrix composites (MMCs), and polymer matrix composites (PMCs). Polymer matrix composites containing fibers, such as carbon and glass, are quite commonly used as engineering materials. Metals containing ceramic particles, whiskers, short or long fibers also attract attention in view of their high temperature capabilities. The ceramic matrix composites are the newest entrants in the composite field, and have the highest service temperature range, excellent hardness, and stiffness (Chawla, 1993). The ultimate performance of the composite may be determined by: (1) the choice of individual constituents, in regard to their synthesis and chemical compositions; (2) the processing required to produce the composite; (3) the mechanical behavior of the composite; and (4) the interface region between matrix and reinforcement, to name a few.

4.1.2 *Short fiber-reinforced composites*

Fibers, because of their small cross-sectional dimensions, are not directly usable in engineering applications. They are, therefore, embedded in matrices to form fibrous composites. In PMCs and MMCs, the matrix serves to bind the fibers together, transfer loads to the fibers, and protect fibers from environmental attack and damages due to handling, while the fibers are responsible for achieving higher strength and stiffness by transferring the loads applied on the composite (Agarwal, *et al*, 1990). Reinforcing fibers in composite may be short or long in comparison with composite's overall dimensions. Composites with short fibers are called discontinuous or short fiber-reinforced composites and those with long fibers are classified as continuous fiber-

reinforced composites. A further distinction is that a short fiber-reinforced composite can be considered as one in which the fiber length affects the properties of the composite. In short-fiber composites, the load transfer function of the matrix is more critical than in continuous fiber-reinforced composites. Loads are not directly applied on the fiber but are applied to the matrix material and then transferred to the fibers through the fiber ends and also through the cylindrical surface of the fiber. When the length of a fiber is much greater than the length over which the transfer of stress takes place, the end effects can be neglected and the fiber may be considered to be continuous. In case of short fiber-reinforced composite, the end effects cannot be neglected and the composite properties are a function of fiber length.

4.1.3 *Unidirectional fibrous composites*

A unidirectional fibrous composite consists of aligned fibers embedded in a matrix. The direction that is parallel to fibers is generally called the *longitudinal direction*. The direction perpendicular to the fibers is called the *transverse direction*. A unidirectional fibrous composite shows different properties in the longitudinal and transverse directions. Usually, the unidirectional fiber-reinforced composites are very strong and stiff in the longitudinal direction but generally weak and compliant in the transverse direction. In the present work, the longitudinal Young's modulus of unidirectional discontinuous fiber-reinforced composite is determined by FEM, and the results are compared with those obtained from the modified shear lag model (Hsueh, 2000).

4.2 Literature Review

One of the earliest attempts to obtain an analytical solution to the stress transfer in fiber-reinforced composites is given by Cox (1952), and his model is now referred to as the classical shear lag model in which a straight, circular cylindrical, discontinuous fiber embedded in a concentric cylindrical matrix is considered. The classical shear lag model was elegant in its simplicity and provides accurate estimates of the increase in elastic modulus due to fibers when the fiber aspect ratio is sufficiently large. However, the major shortcoming of the model is its inability to provide sufficiently accurate predictions of increase in composite elastic modulus when the fiber aspect ratio is small. The predicted composite modulus by the classical shear lag model is substantially smaller than the experimentally measured modulus in the regime of small fiber aspect ratio, which is applicable to the majority of current short fiber-reinforced or whisker-reinforced composites. The underestimation of composite modulus by the classical shear lag model results from its neglect of normal stress transfer at fiber ends and the stress intensification in the matrix region near the fiber (Kim and Nair, 1990).

Rigorous elasticity models based on variational principles (Hashin and Shtrikman, 1962, 1963) and the self-consistent method (Hill, 1965a) are developed in order to predict the increase in effective elastic modulus of short fiber-reinforced composites in the small fiber aspect ratio regime. Though the variational method originally developed by Paul (1960) provides proper bounds on the effective elastic moduli, it does not provide proper bounds the local stress values in the fiber and surrounding matrix. The self-consistent model is first developed by Hershey (1954) and

Kroner (1958) to model the behavior of polycrystalline materials and is extended to multiphase media by Hill (1965b) and Budiansky (1965). The self-consistent method is based on the equivalent inclusion method by Eshelby (1957), who solved for the elastic field of a single inhomogeneity embedded in an infinite medium.

Muki and Sternberg (1969) and Sternberg and Muki (1970) use a shear-lag approach in a more refined manner involving integro-differential equations. They have calculated the local stresses inside the fiber. However, the model assumes that the stress at fiber center is given by the rule of mixtures, which is strictly applicable only to the long fiber case. Furthermore, Sternberg's results are not able to be applied to obtain expressions for the matrix stress intensification in the fiber end region, which provides a significant contribution to the stiffness.

Nardone and Prewo (1986) and Nardone (1987) attempt to modify the classical shear lag model by assuming that both the fiber end stress and the matrix average stress are equal to the matrix yield stress. They developed an approximate estimate of the increase in composite yield strength. The approach is, however, not applicable to the purely elastic regime wherein the increase in elastic modulus is of interest.

Taya and Arsenault (1989) attempt to modify the original shear lag approach by assuming that the stress concentration at the fiber ends can be ignored. Kim and Nair (1990) modify the shear lag analysis by using the finite element analysis (FEA) to determine the normal stress at the fiber ends. Their results of the predicted modulus increase in short-fiber composites show a good agreement with FEA results as well as experimental data. While their work demonstrates that shear lag solutions can be applied

to short fiber-reinforced composites provided that fiber end effects are account for, the model relies heavily on FEA.

Nair and Kim (1992) develop a rigorous modification of the original shear lag analysis so as to retain its accuracy at small fiber aspect ratio. Closed-form solutions to the modulus increases and the local tensile and shear stress values in the matrix and fiber are determined. However, this model in general overestimates the effective Young's Modulus of short fiber-reinforced composites, especially when fiber aspect ratio is more than 5

Tucker and Liang (1998) compare the results from existing models with those from FEA. Mori-Tanaka model is suggested to be the best choice for estimating the stiffness of aligned short fiber-reinforced composites. Shear lag based models are believed to be able to give good predictions on the longitudinal Young's modulus of composites with fiber aspect ratios greater than 10, provided that a proper choice of the representative volume element is made.

Hsueh and his coworkers study the stress transfer and estimate Young's moduli of discontinuous fiber-reinforced composites in a series of work; see Hsueh (1989, 1995, 2000), Hsueh and Becher (1996), and Hsueh *et al* (1997) In order to improve the shear lag model to give better predictions on both Young's moduli and the stress transfer phenomena in short fiber-reinforced composites, a rigorous modified shear lag model is developed by judiciously selecting the representative volume element. The predicted stress distribution along the fiber length during uniaxial loading of the composite is compared with those obtained by FEA (Zhang, 1999). Also by a judicious choice of the

representative volume element for the modified shear lag model, the predicted Young's moduli of the composite agrees very well with those predicted from Halpin-Tsai semi-empirical equation, Eshelby model, and a numerical analysis based on finite-difference method (Hsueh, 2000).

4.3 Scope of Study

Longitudinal Young's modulus is one of the most important elastic constants for engineering materials. Theoretical analyses of Young's modulus of composites may be classified into four types: semi-empirical formulations, models based on Eshelby (1957), the shear lag models, and the numerical methods. Among the four types of analyses, the shear lag model is considered to be the least accurate one due to its crude approximations in the analysis. However, closed-form shear lag models are practically popular due to simplicity. They are also the only ones to examine stress transfer between the fiber and the matrix during the loading of the composite. In order to improve the shear lag model to predict Young's moduli of the aligned short fiber-reinforced composites more accurately, a modified shear lag model has been developed by Hsueh (2000), which is referred to as the modified shear lag model in the present work. In the present study, FEA is performed to examine the accuracy of the Hsueh's latest modified shear lag model. It is assumed that.

- (1) The fibers and the matrix are linearly elastic, the matrix is isotropic, and the fibers are either isotropic or transversely isotropic;

- (2) The fibers are axisymmetric and can be characterized by an aspect ratio l/a , i.e. ratio of length to diameter of the fiber;
- (3) The fibers and the matrix are well bonded at their interface, and remain that way during deformation. Thus, it is not necessary to consider interfacial slip, fiber/matrix debonding, or matrix microcracking

CHAPTER 5

FEA ON EFFECTIVE YOUNG'S MODULUS OF SHORT FIBER-REINFORCED COMPOSITES

While the validity of the modified shear lag model (Hsueh *et al.*, 1997) on stress transfer between the short fiber and matrix is verified by FEA (Zhang, 1999). The present work is focused on examining the accuracy of the modified shear lag model's prediction of longitudinal Young's moduli (Hsueh, 2000) of short fiber-reinforced composites, using FEA.

5.1 Geometric and Material Models

The stress distribution and the deformation of the discontinuous fiber-reinforced composites are simulated by use of the geometric model shown in Figure. 5.1 A two-dimensional projection of the mid-plane of the geometric model is shown in Figure 5.2. When a fiber with radius a and length $2l$ is embedded in a concentric cylindrical matrix with radius b and length $2l'$. The cylindrical coordinate system (r, θ, z) is used. Both the matrix and the fiber are assumed to be linearly elastic until failure. In addition, the matrix as well as the fiber is assumed to be free of any micro-defects, such as voids and cracks. Furthermore, the fiber and the matrix are assumed to be perfectly bonded at both the fiber ends ($z = \pm l$) and at the circumferential interface ($r = a$) so that no slippage can occur at the interface.

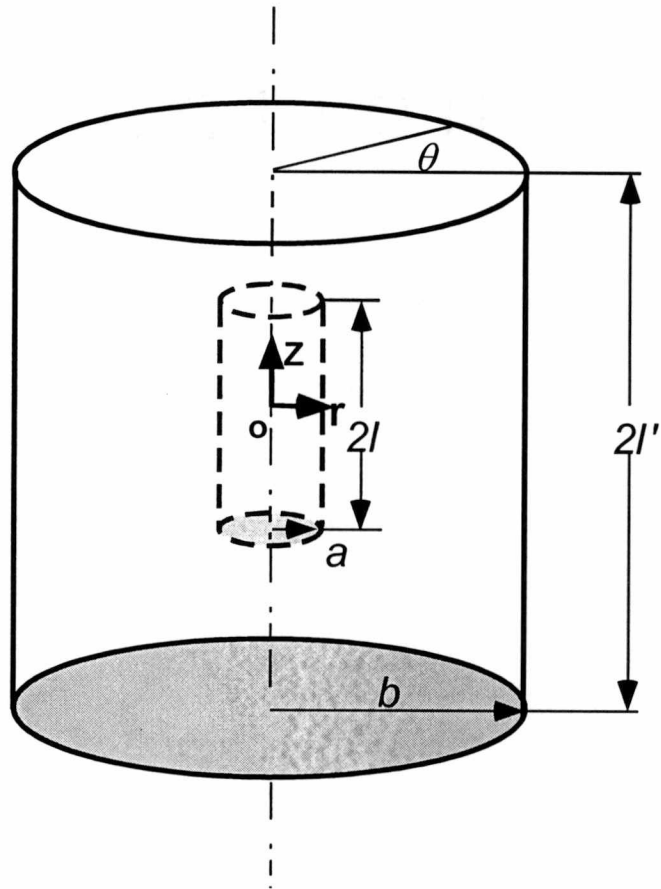


Figure 5.1: Geometric model representing a single circular cylindrical fiber embedded in a concentric circular cylindrical matrix.

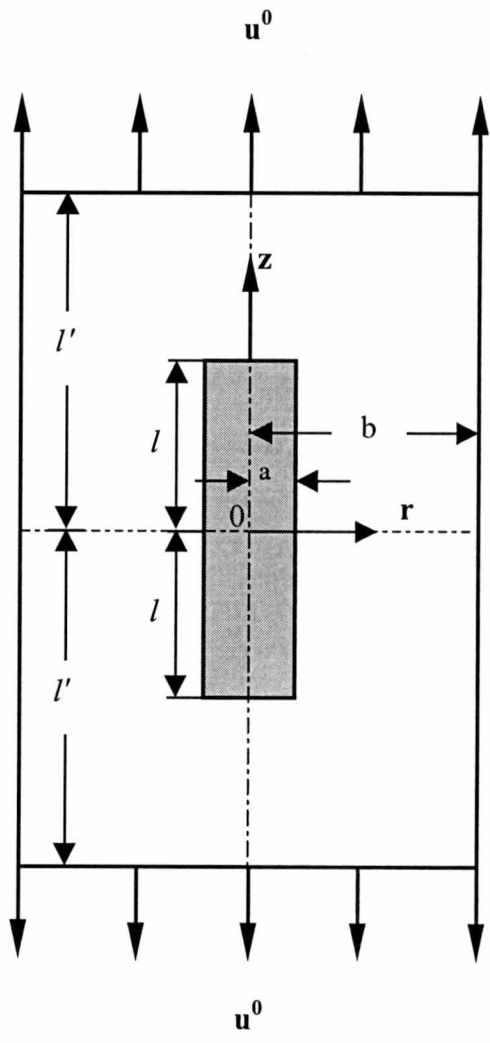


Figure 5.2: Two-dimensional projection of a single circular cylindrical fiber embedded in a concentric cylindrical matrix.

5.2 Governing Equations and Boundary Conditions

In the absence of body forces, the stresses in a general three-dimensional body must satisfy the following equations of equilibrium in cylindrical coordinate system (Timoshenko and Goodier, 1970):

$$\frac{\partial \sigma_r}{\partial r} + \frac{1}{r} \frac{\partial \tau_{r\theta}}{\partial \theta} + \frac{\partial \tau_{rz}}{\partial z} + \frac{\sigma_r - \sigma_\theta}{r} = 0 \quad (5.1a)$$

$$\frac{\partial \tau_{rz}}{\partial r} + \frac{1}{r} \frac{\partial \tau_{z\theta}}{\partial \theta} + \frac{\partial \sigma_z}{\partial z} + \frac{\tau_{rz}}{r} = 0 \quad (5.1b)$$

$$\frac{\partial \tau_{r\theta}}{\partial r} + \frac{1}{r} \frac{\partial \sigma_\theta}{\partial \theta} + \frac{\partial \tau_{\theta z}}{\partial z} + \frac{2\tau_{r\theta}}{r} = 0 \quad (5.1c)$$

where σ_r , σ_θ and σ_z are the radial, tangential, and axial stress components, respectively, whereas $\tau_{r\theta}$ ($=\tau_{\theta r}$), $\tau_{\theta z}$ ($=\tau_{z\theta}$), and τ_{rz} ($=\tau_{zr}$) are the shear stress components.

If the material is linearly elastic and isotropic, the normal strains in the radial, tangential, and axial directions, ε_r , ε_θ , and ε_z , and the shear strain $\varepsilon_{r\theta}$ ($=\varepsilon_{\theta r}$), $\varepsilon_{\theta z}$ ($=\varepsilon_{z\theta}$), and ε_{rz} ($=\varepsilon_{zr}$), are related to stresses by the generalized Hooke's law as follows:

$$\varepsilon_r = \frac{1}{E} [\sigma_r - \nu(\sigma_z + \sigma_\theta)] \quad (5.2a)$$

$$\varepsilon_\theta = \frac{1}{E} [\sigma_\theta - \nu(\sigma_z + \sigma_r)] \quad (5.2b)$$

$$\varepsilon_z = \frac{1}{E} [\sigma_z - \nu(\sigma_r + \sigma_\theta)] \quad (5.2c)$$

$$\varepsilon_{r\theta} = \frac{1+\nu}{E} \tau_{r\theta} \quad (5.2d)$$

$$\varepsilon_{rz} = \frac{1+\nu}{E} \tau_{rz} \quad (5.2e)$$

$$\varepsilon_{\theta z} = \frac{1+\nu}{E} \tau_{\theta z} \quad (5.2f)$$

where E , and ν are Young's modulus and Poisson's ratio of the material, respectively. In case of composite materials, E and ν are functions of position.

The composite is subjected to a prescribed displacement, u^0 , at $z = \pm l'$. Since the geometry and the loading conditions are axisymmetric, the tangential displacement component, u_θ , vanishes, and the radial and axial displacement components, u_r and u_z , are independent of θ . That is,

$$u_r = u_r(z, r) \quad u_\theta = 0 \quad u_z = u_z(z, r) \quad (5.3a-c)$$

Thus the infinitesimal normal and shear strain components can be defined by

$$\varepsilon_r = \frac{\partial u_r}{\partial r} \quad \varepsilon_\theta = \frac{u_r}{r} \quad \varepsilon_z = \frac{\partial u_z}{\partial z} \quad (5.4a-c)$$

$$\varepsilon_{r\theta} = 0 \quad \varepsilon_{rz} = \frac{1}{2} \left(\frac{\partial u_r}{\partial z} + \frac{\partial u_z}{\partial r} \right) \quad \varepsilon_{z\theta} = 0 \quad (5.4d-f)$$

Equations of equilibrium, Eq. (5.1a-b) become

$$\frac{\partial \sigma_r}{\partial r} + \frac{\partial \tau_{rz}}{\partial z} + \frac{\sigma_r - \sigma_\theta}{r} = 0 \quad (5.5a)$$

$$\frac{\partial \tau_{rz}}{\partial r} + \frac{\partial \sigma_z}{\partial z} + \frac{\tau_{rz}}{r} = 0 \quad (5.5b)$$

It is noted that Eq. (5.1c) is automatically satisfied

The boundary conditions for the present model are given by

$$u_z = u^0 \quad \text{at } z = \pm l', \quad 0 \leq r \leq b \quad (5.6a)$$

$$\sigma_r = \tau_{rz} = 0 \quad \text{at } r = b, \quad -l' \leq z \leq l' \quad (5.6b)$$

5.3 Finite Element Model

Due to symmetry about the z- and r- axes in Fig. 5.2, the FEA model used in the present work considers only one quarter of the actual physical model, see Fig. 5.3. The finite element package used is ABAQUS together with pre- and post-processor PATRAN. Two-dimensional eight-node, biquadratic axisymmetric elements are used; see Fig. 5.4. A 1-radian segment of the cylinder represented by the rectangle domain, ABCD, in Figure 5.3 is analyzed. Typically, 2000 elements are used. Such a fine mesh is found to be necessary to obtain radial stress continuity across the interface. An axial displacement is prescribed at the nodes along the top, DC. The sides AB and AD are

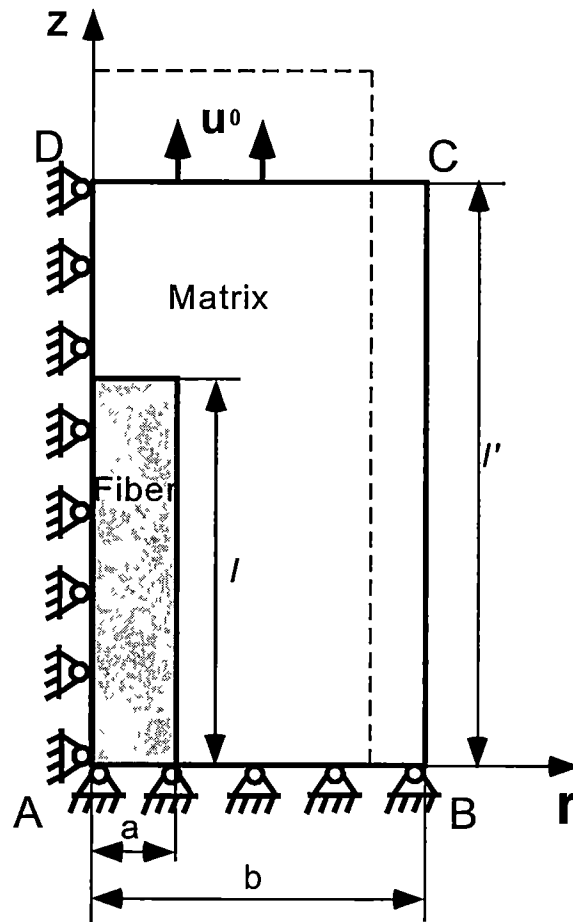


Figure 5.3 FEA model considering only one quarter of the actual physical model, with the deformed shape shown by dashed lines.

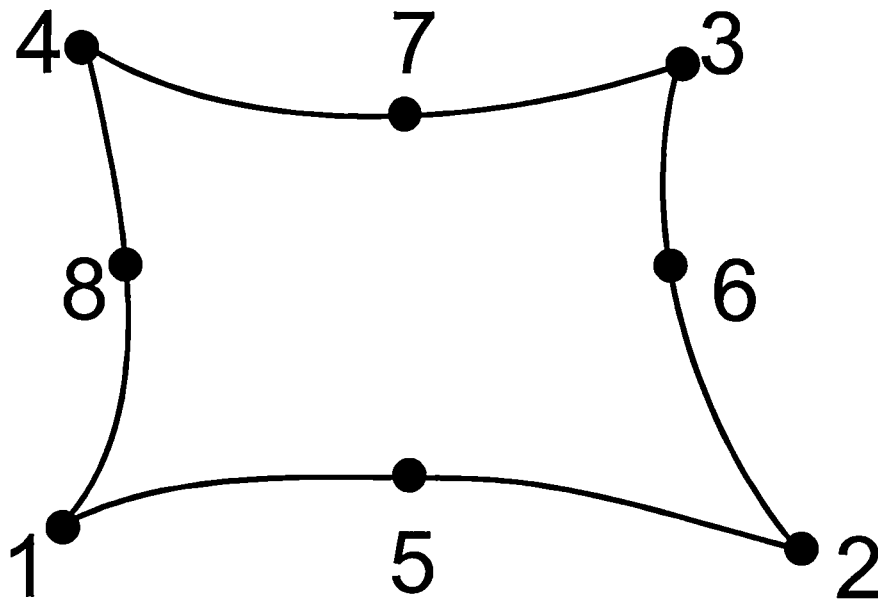


Figure 5 4: Two-dimensional eight-node, biquadratic axisymmetric element in ABAQUS.

restricted to satisfy the symmetry conditions. The shape of the deformed grid is indicated in Figure 5.3 by the dashed lines. A typical mesh generated by PATRAN, employed in the present FEA, is given in Figure 5.5. It is noted that large elements are used where the stress are relatively constant, and smaller elements are employed when the stress gradient becomes dramatic. To this end, many elements appear in a small area near the end of the fiber and fiber/matrix where stress concentration and/or dramatic stress transfer is expected. The boundary conditions for the finite element model are given by

$$u_r = 0, \tau_{rz} = 0 \quad \text{at } r = 0, 0 \leq z \leq l' \quad (5.7a)$$

$$u_z = 0, \tau_{rz} = 0 \quad \text{at } z = 0, 0 \leq r \leq b \quad (5.7b)$$

$$u_z = u^0 \quad \text{at } z = l', 0 \leq r \leq b \quad (5.7c)$$

$$\sigma_r = 0, \tau_{rz} = 0 \quad \text{at } r = b, 0 \leq z \leq l' \quad (5.7d)$$

5.4 Results and Discussion

It is noted that only the fiber aspect ratio and the volume fraction are needed in using most of the existing analytic models such as Halpin-Tsai and Eshelby model to predict longitudinal Young's modulus of the aligned short fiber-reinforced composites. However, the specific dimensions of the representative volume element (RVE) are required in using the modified shear lag model (Hsueh, 2000) because a specific fiber volume fraction may involve different combinations of a , l , b and l' . To this end, a simple criterion for selecting the RVE is established (Hsueh, 2000):

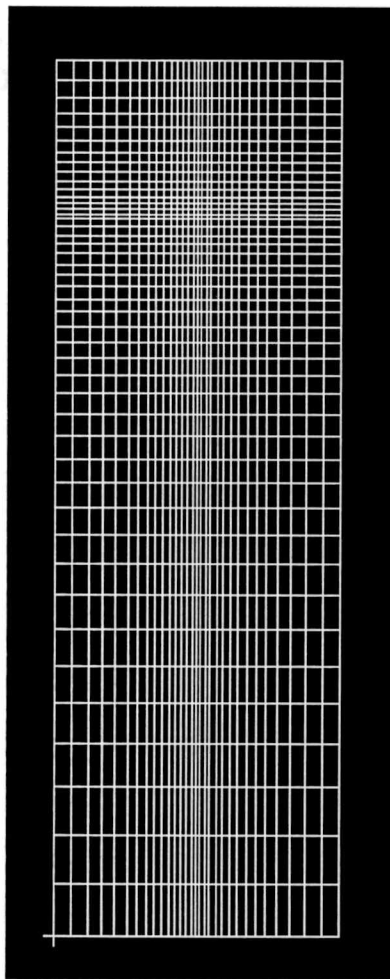


Figure 5.5: A typical mesh generated by PATRAN, employed in the present FEA.

$$b = af^{-p} \quad l' = lf^{2p-1} \quad (5.8a, b)$$

where, p is given by

$$p = \frac{1}{2} - \frac{1}{6} \exp\left(\frac{-l}{5a}\right) \quad (5.9)$$

First, a model composite consisting of an aluminum (Al) matrix embodying a single silicon carbide (SiC) fiber is considered. The radius of the fiber is chosen to be 1 mm, and the fiber aspect ratio is assumed to range from 1 to 30. By setting the volume fraction of the fiber to be 0.1, 0.2, and 0.3 respectively, the radius of the matrix, and the length of the fiber and the matrix are readily obtained by Eq. (5.8a, b) and Eq. (5.9). The elastic properties of the fiber and the matrix, both of which are assumed to be isotropic, are shown in Table 5.1 (Hsueh, 2000).

Table 5 1: Constituent properties of Al/SiC composite (Hsueh, 2000).

Material	Young's modulus (GPa)	Poisson's ratio
Al (matrix)	72	0.3
SiC (fiber)	450	0.2

The composite is loaded by applying prescribed longitudinal displacement, u^0 , to all of the nodal points on the top surface of the matrix. The value of displacement chosen is 0.002 times of the length of the matrix. This corresponds to a normal strain of the composite, $\bar{\varepsilon}_z$, given by

$$\bar{\varepsilon}_z = u^0 / l' = 0.002 \quad (5.10)$$

The average axial stress on the top surface of the matrix is given by

$$\bar{\sigma}_z = \frac{\int_0^b 2\pi r \sigma(r) dr}{\pi b^2} \approx \frac{\sum A_i \sigma_i}{A_{total}} \quad (5.11)$$

where N is the total number of elements used for the top surface of the cylinder, A_i indicates the area of the i th element subjected to the axial stress σ_i , and A_{total} is the total area of the composite end, given by

$$A_{total} = \sum A_i = \pi b^2 \quad (5.12)$$

The longitudinal Young's modulus of the composite is defined by

$$E_c = \frac{\bar{\sigma}_z}{\bar{\epsilon}_z} \quad (5.13)$$

Figures 5.6~5.8 give the longitudinal Young's modulus of the SiC/Al composite, E_c , as a function of fiber aspect ratio, l/a , for fiber volume fraction of 0.2, 0.1 and 0.3, respectively. Results obtained from modified shear lag modulus (Hsueh, 2000) are also shown in Figures 5.6~5.8 for comparison. It is noted that the two methods agree quite well with each other, especially when the fiber aspect ratio is less than 10. When (1) $f = 0.2$ and $l/a = 1.5$ and 9.9 , (2) $f = 0.1$ and $l/a = 1.6$ and 8.1 , (3) $f = 0.3$ and $l/a = 1.6$ and 7.5 ; the modified shear-lag and the present FEA yield the same results. In comparison with FEA, the modified shear lag model first overestimates and then as the fiber aspect ratio increases, underestimates the longitudinal Young's modulus of the composite.

Another model composite consisting of a single SiC fiber embedded in an Al 2124, 6061 or 8090 matrix, is considered. The elastic properties of the fiber and the matrix, both of which are assumed to be isotropic, are listed in Table 5.2 (Hsueh, 2000).

Table 5.2 Properties of SiC particulate- or whisker-reinforced aluminum matrix composites (Hsueh, 2000).

Composite	Reinforcement	E_f (GPa)	E_m (GPa)	ν_f	ν_m	aspect ratio, l/a
SiC/2124 (T4*)	particulate	450	72	0.2	0.3	1.6
SiC/6061 (T6**)	particulate	450	71.7	0.2	0.3	3
SiC/8090 (T6**)	whisker	480	78.2	0.2	0.3	4

*T4: room temperature aged, **T6: heat treated

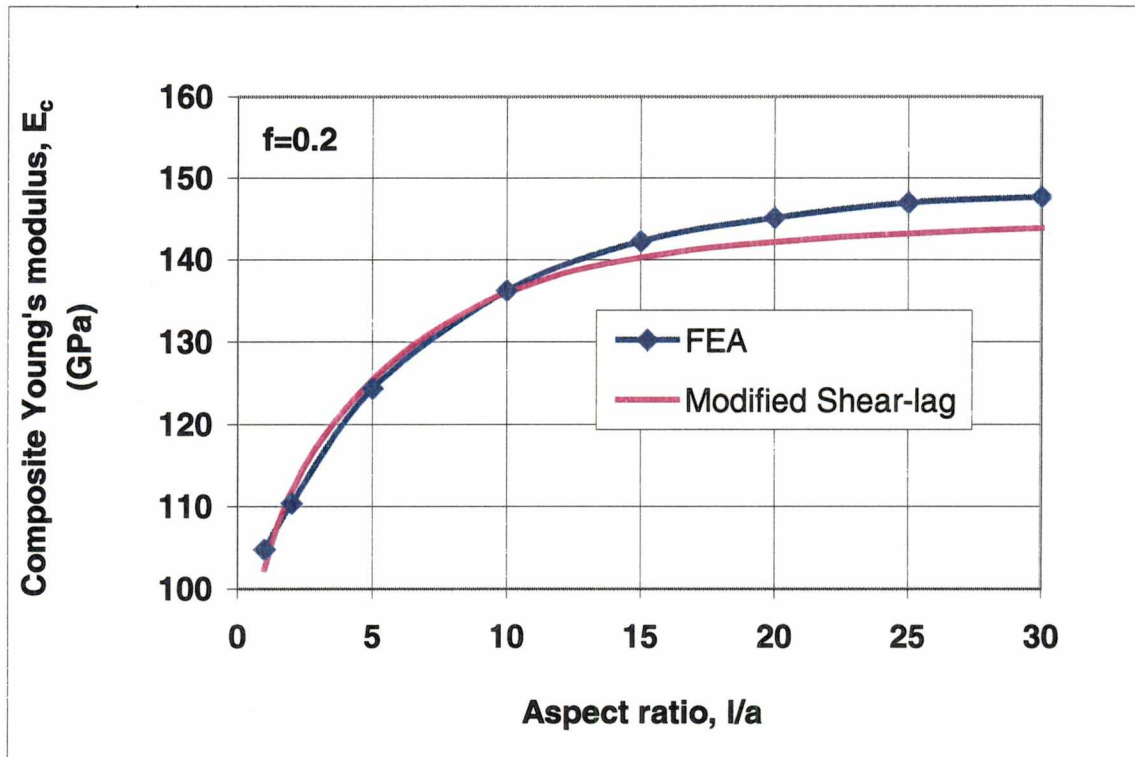


Figure 5.6: Effective Longitudinal Young's modulus, E_c , of 20%-SiC/Al composite, as a function of fiber aspect ratio, l/a .

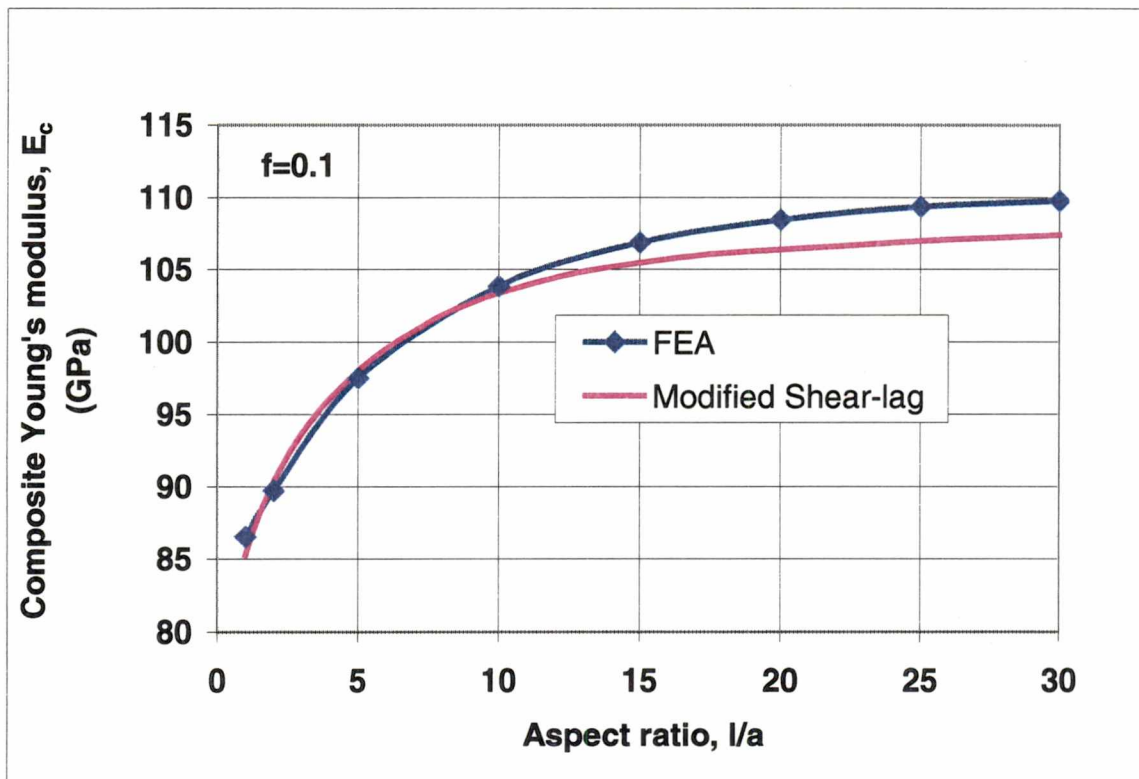


Figure 5.7: Effective Longitudinal Young's modulus, E_c , of 10%-SiC/Al composite, as a function of fiber aspect ratio, l/a .

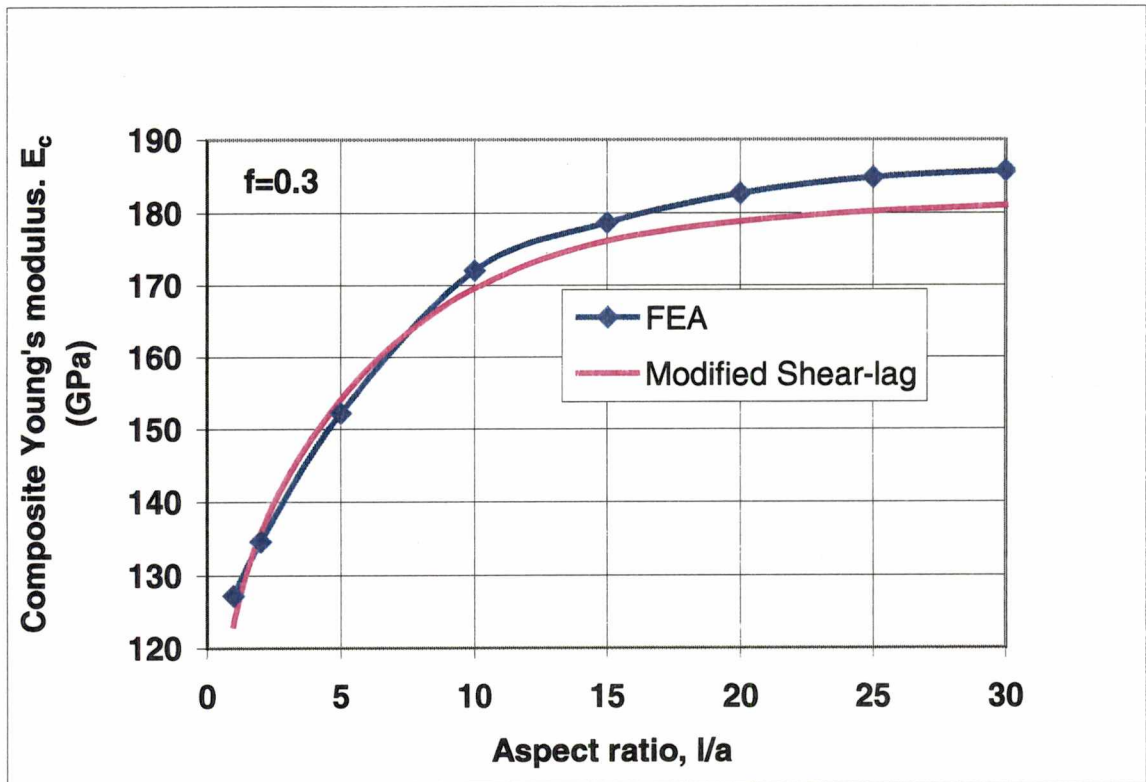


Figure 5.8: Effective Longitudinal Young's modulus, E_c , of 30%-SiC/Al composite, as a function of fiber aspect ratio, l/a .

Figures 5 9~5 11 present the effective longitudinal Young's modulus, E_c , as a function of fiber volume fraction, f , for SiC/Al 2124, SiC/Al 6061 and SiC/Al 8090 composite with fiber aspect ratio, l/a , of 1.6, 3 and 4, respectively. It is seen that the results from the modified shear lag model are almost identical with those obtained from the FEA model. The comparison demonstrates that the modified shear lag model (Hsueh, 2000) is quite accurate in predicting the longitude Young's modulus of short fiber-reinforced composites with fiber aspect ratio ranging from 1.6 to 4. It is noted that other shear lag based models fail to accurately predict the longitude Young's modulus of short fiber-reinforced composites with fiber aspect ratio less than 4. The success of Hsueh (2000) may be due to its judicious selection of RVE, i.e., Eq. (5.8a, b) and (5.9)

At last, a RVE that has the same aspect ratio as that of the fiber, i.e. $l'/b = l/a$, is considered in a 20%-SiC/Al composite. For the special case of $l'/b = l/a$, the modified shear lag model agrees well with FEA when $l/a < 2$ or $l/a > 15$. In this particular case, the modified shear lag model in general underestimates the longitudinal Young's modulus of the 20%-SiC/Al composite, see Figure 5 12.

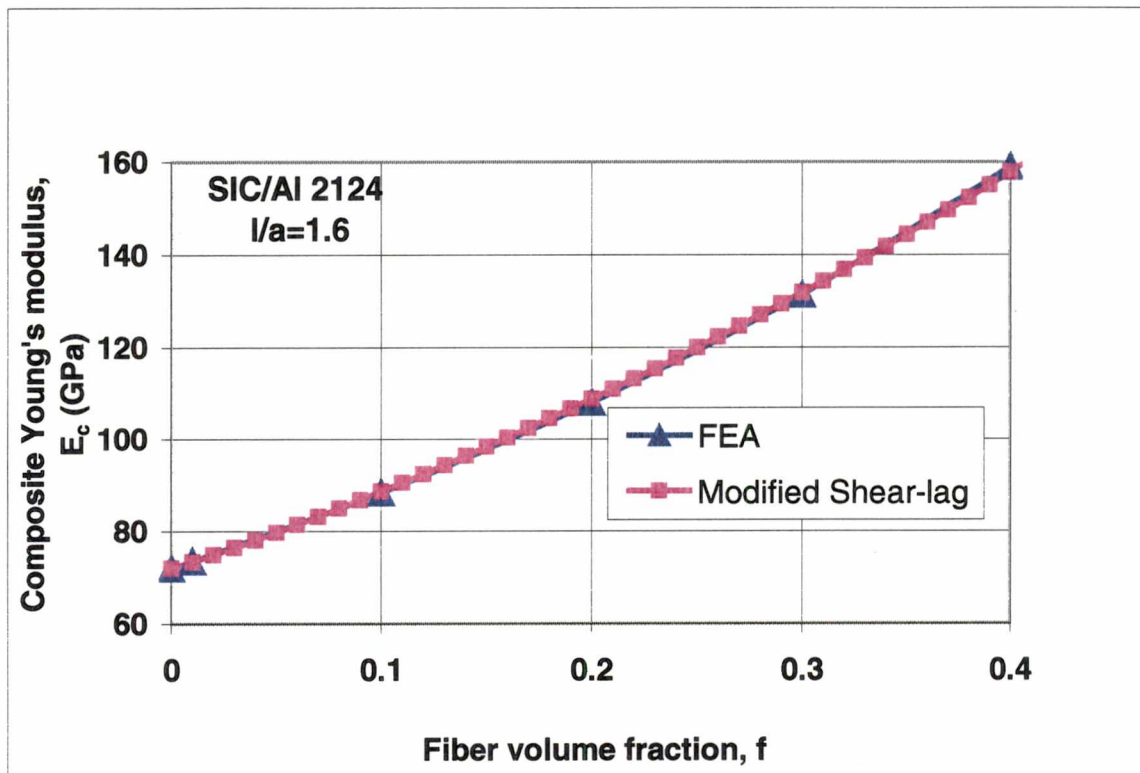


Figure 5.9: Effective Longitudinal Young's modulus, E_c , of SiC/2124 composite, as a function of fiber volume fraction, f , for fiber aspect ratio, $l/a = 1.6$.

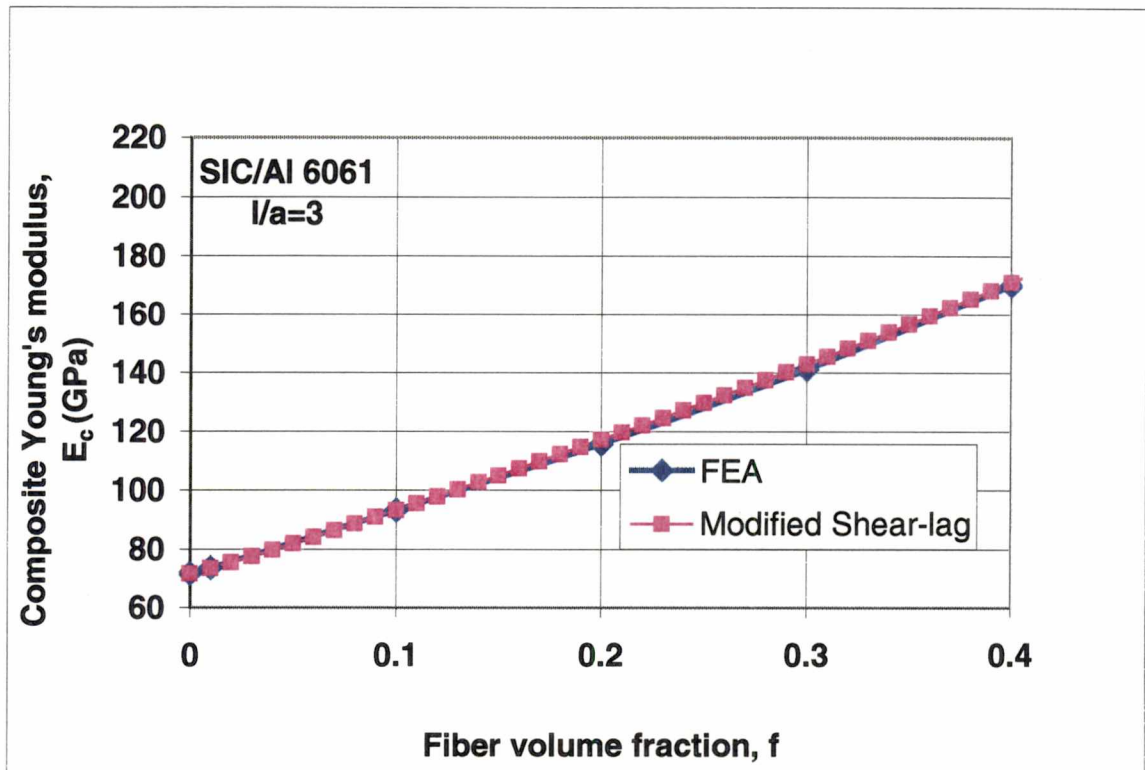


Figure 5.10: Effective Longitudinal Young's modulus, E_c , of SiC/6061 composite, as a function of fiber volume fraction, f , for fiber aspect ratio, $l/a = 3$.

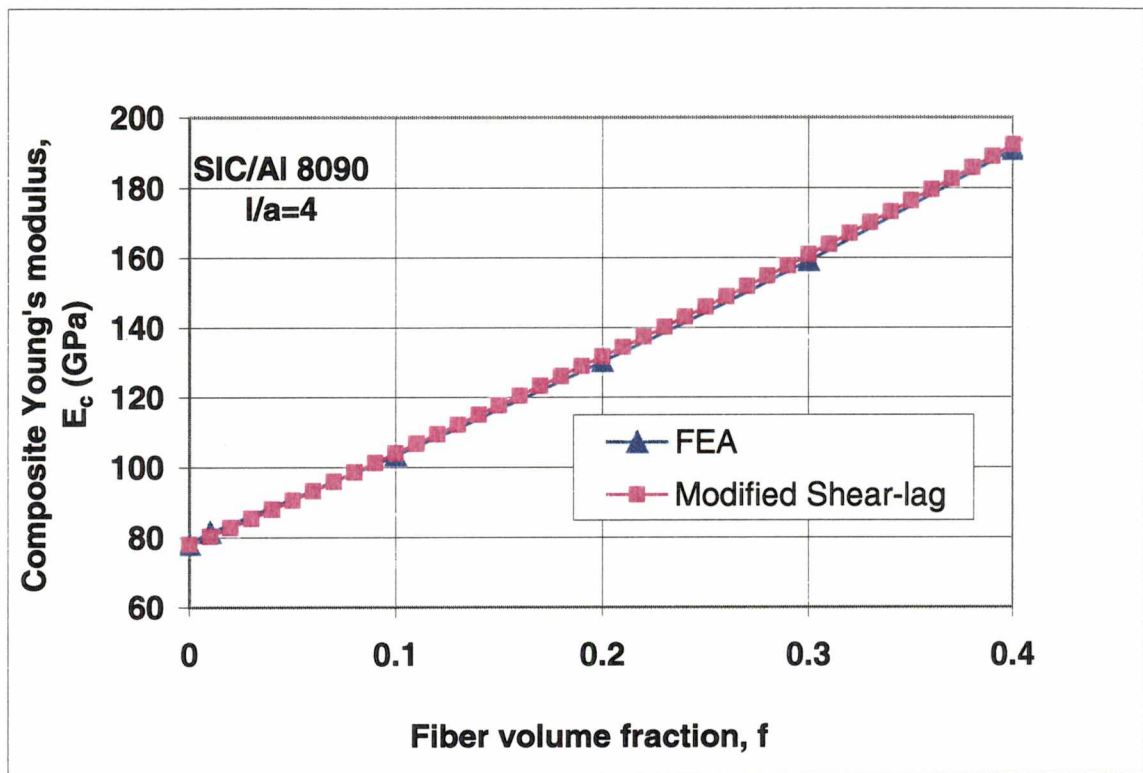


Figure 5.11: Effective Longitudinal Young's modulus, E_c , of SiC/8090 composite, as a function of fiber volume fraction, f , for fiber aspect ratio, $l/a = 4$.

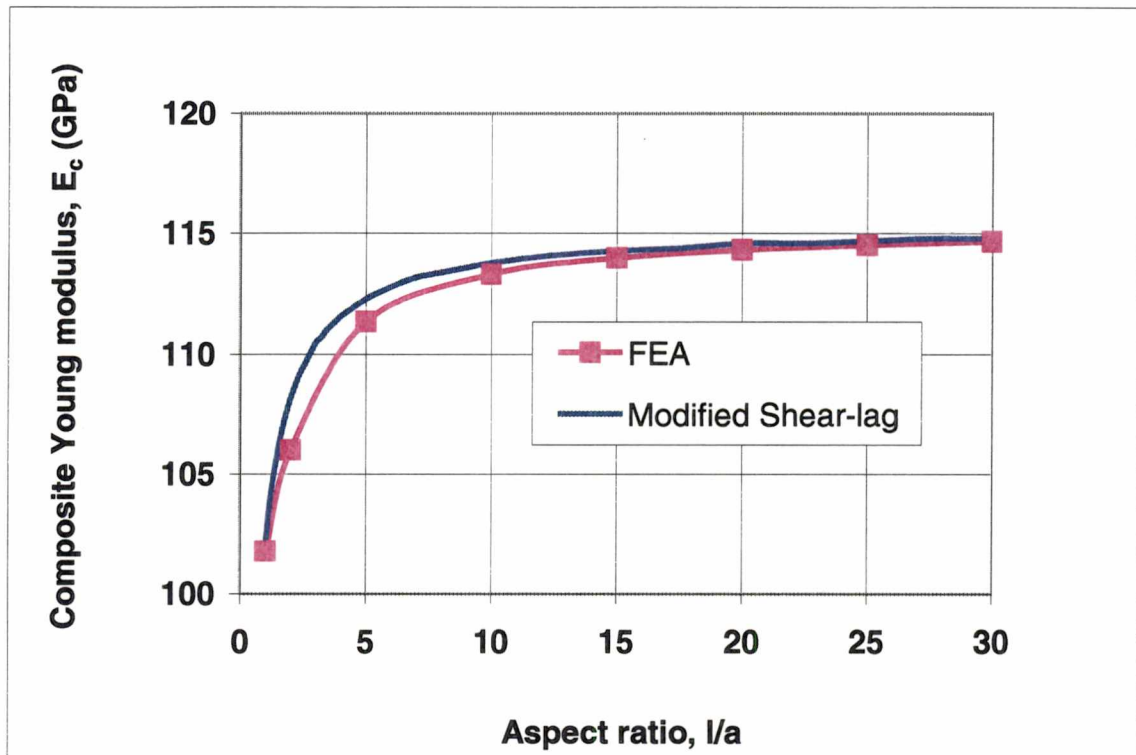


Figure 5.12: Effective Longitudinal Young's modulus, E_c , of 20%-SiC/Al composite, as a function of fiber aspect ratio, l/a , for $l/a = l'/b$.

CHAPTER 6

CONCLUSION AND DISCUSSIONS

The classical shear lag model, which considers a composite consisting of a circular cylindrical fiber embedded in a concentric cylindrical matrix, assumes that:

- (1) The fiber end is debonded with the matrix, i.e. no load transfer through the fiber end, and
- (2) The fiber carries only the axial load, and the matrix surrounding the fiber transmits only the shear stress.

The above approximation leads to inaccuracy on stress transfer between the fiber and the matrix in short fiber-reinforced composites, as well as the prediction of the longitudinal Young's modulus of the short fiber-reinforced composites

Several modified shear lag models are developed to determine the stress field in the neighborhood of fiber ends. Among these modified shear lag models, the model by Hsueh *et al* (1997) is creative in adding imaginary fibers with the matrix properties to the (real) fiber ends, and consequently predicts the stress transfer in short fiber-reinforced composites accurately.

Moreover, Hsueh (2000) further modified his shear-lag model by judiciously defining the model geometry using Eq. (5 8 a~b) and Eq. (5 9) to improve the prediction of effective longitudinal Young modulus of short fiber-reinforced composites.

In comparison with the present FEA model, one finds that the modified shear lag model is able to give good prediction on longitudinal Young's modulus of short fiber-

reinforced composites with fiber aspect ratio ranging from 1 to 10, which is the typical range of fiber aspect ratio for short fiber-reinforced composites.

Specifically the two methods give very close results, when (1) $f = 0.2$ and $l/a = 1.5$ or 9.9 ; (2) $f = 0.1$ and $l/a = 1.6$ or 8.1 ; and (3) $f = 0.3$ and $l/a = 1.6$ or 7.5 . In between these two aspect ratios, the modified shear lag model overestimates the longitudinal Young modulus of the short fiber-reinforced composites and underestimates E_c otherwise.

One also finds that the longitudinal Young's moduli of short fiber-reinforced composites predicted by the modified shear lag model are almost identical with those from FEA when the fiber aspect ratio ranges from 1.6 to 4. It should be noted from the literature that most shear lag models fail to accurately predict the longitudinal Young's modulus of short fiber-reinforced composite with fiber aspect ratio less than 4 (Nair and Kim, 1992).

When the fiber aspect ratio (l/a) is equal to the composite aspect ratio (l'/b), the modified shear lag model gives excellent agreement with FEA for $l/a < 2$ or $l/a > 10$. The discrepancy, however, is significant, when $l/a \sim 3$.

Another thing worthy of mention is that when applying uniaxial tension, rather than prescribed displacement, the calculated longitudinal Young's moduli of the composites by averaging strain over the top surfaces of the composites are much higher than those obtained from the modified shear lag model and the present FEA model. The reason may be that the two boundary-value problems are in essence different.

REFERENCES

REFERENCES

- Agarwal, B. D and Broutman, L. J (1990), *Analysis and Performance of Fiber Composites*, Second Edition, John Wiley & Sons, Inc.
- Amiri, A. and Vafai, K. (1994), "Analysis of dispersion effects and non-thermal equilibrium, non-Darcian, variable porosity incompressible flow through porous media," *International Journal of Heat and Mass Transfer*, **37**, pp. 939-954.
- Antohe, B. V , Lage, J L., Prince, D. C and Weber, R M. (1996), "Numerical Characterization of Micro Heat Exchangers using Experimentally Tested Porous Aluminum Layers," *International Journal of Heat and Mass Transfer*, **17**, pp. 594-603.
- Bastawros, A. F , Evans, A. G and Stone, H A (1999), "Evaluation of Cellular Metal Heat Transfer Media," *Harvard University Report*, **MECH 325**, Cambridge.
- Bejan, A. (1993), *Heat Transfer*, John Wiley & Sons, Inc.
- Bejan, A and Morega, A. M. (1993), "Optimal Arrays of Pin Fins and Plate Fins in Laminar Force Convection," *Journal of Heat Transfer*, **115**, pp. 75-81.
- Bell, K. J. (1990), "Introduction to Heat Exchanger Design," *Hemisphere Handbook of Heat Exchanger Design*, Editors: Hewitty, G. F., Hemisphere Publishing Corporation, New York, pp. 3.1.1-3 1 49.
- Budiansky, B (1965), "On the Elastic Modulus of Some Heterogeneous Materials," *Journal of Mechanics and Physics of Solids*, **13**, pp. 223-227.

- Chawla, K. K. (1993), *Ceramic Matrix Composites*, Chapman & Hall, London, pp 1-10, 317-337
- Coppage, J. E. (1952), "Heat Transfer and Flow Friction Characteristics of Porous Media," *TR-No 16, Office of Naval Research Contract N6onr 251 Task 6*, Department of Mechanical Engineering, Stanford University.
- Coppage, J. E. and London, A. L. (1956), "Heat Transfer and Flow Friction Characteristics of Porous Media," *Chemical Engineering Progress*, **52**, pp. 57-63.
- Cox, H. L. (1952), "The Elasticity and Strength of Paper and Other Fibrous Materials," *British Journal of Applied Physics*, **3**, pp 72-79.
- DeHoff, R. T. and Rhines, F. N. (1968), *Quantitative Microscopy*, McGraw-Hill Book Company, NY.
- Dullien, F. A. L. (1992), *Porous Media Fluid Transport and Pore Structure*, Second Edition, Academic
- Eshelby, J. D. (1957), "The Determination of the Elastic Field of an Ellipsoidal Inclusion, and Related Problems," *Proceedings of the Royal Society of London*, **A241**, pp 376-396.
- Gibson, L. J. and Ashby, M. A. (1997), *Cellular Solids Structure and Properties*, Second Edition, Cambridge University Press.
- Gosse, J. (1981), *Technical Guide to Thermal processes*, Cambridge University Press.
- Hager, J. W. and Lake, M. L. (1992), "Novel Hybrid Composites Based on Carbon Foams," *Material Research Society Symposium Proceeding*, **270**, pp 29-34.

- Hashin, Z. and Shtrikman, S. (1962), "On Some Variational principles in Anisotropic and Nonhomogeneous Elasticity," *Journal of the Mechanics and Physics of Solids*, **10**, pp 335-332
- Hashin, Z and Shtrikman, S. (1963), "A Variational Approach to the Theory of the Elastic Behavior of Multiphase Materials," *Journal of the Mechanics and Physics of Solids*, **11**, pp. 127-140.
- Hershey, A. V. (1954), "The Elasticity of an Isotropic Aggregate of an Anisotropic Cubic Crystals," *ASME Journal of Applied Mechanics*, **21**, pp. 236-240
- Hewitt, G. F (1990), *Hemisphere Handbook of Heat Exchanger Design*, Hemisphere Publishing Corporation.
- Hill, R (1965a), "Theory of Mechanical Properties of Fiber-Strengthened Materials—III. Self-Consistent Model," *Journal of the Mechanics and Physics of Solids*, **13**, pp. 189-198
- Hill, R. (1965b), "A Self-Consistent Mechanics of Composite Materials," *Journal of the Mechanics and Physics of Solids*, **13**, pp. 213-222
- Holman, J. P. (1989), *Heat Transfer*, Sixth Edition, McGraw-Hill Book Company
- Hsueh, C. H. (1989), "Analytical Analyses of Stress Transfer in Fiber-Reinforced Composites with Bonded and Debonded Fiber Ends," *Journal of Materials Science*, **24**, pp. 4475-4482.
- Hsueh, C. H. (1995), "A Modified Analysis for Stress Transfer in Fiber-Reinforced Composites with Bonded Fiber Ends," *Journal of Materials Science*, **30**, pp. 219-224.

- Hsueh, C. H., (2000), "Young's Modulus of Unidirectional Discontinuous Fiber Composites," *Composite Science and Technology*, in press
- Hsueh, C. H. and Becher, P. F. (1996), "Residual Thermal Stresses in Ceramic Composites, Part II: with Short Fibers," *Material Science and Engineering*, **A212**, pp. 29-35.
- Hsueh, C. H., Young, R. J., Yang, X., and Becher, P. F. (1997), "Stress Transfer in a Model Composite Containing a Single Embedded Fiber," *Acta Metallurgica et Materialia*, **45**, 3, pp. 1469-1476.
- Huang, P. C. and Vafai, K. (1993), "Flow and Heat Transfer Control over an External Surface Using a Porous Block Array Arrangement," *International Journal of Heat and Mass Transfer*, **36**, 16, pp. 4019-4032
- Hunt, M. L. and Tien, C. L. (1988), "Effects of Thermal Dispersion on Forced Convection in Fibrous Media," *International Journal of Heat and Mass Transfer*, **31**, 2, pp. 301-309
- Incropera, F. P. and DeWitt, D. P. (1990), *Fundamentals of Heat and Mass Transfer*, Third Edition, John Wiley and Sons, Inc
- Kakac, S., Shan, R. K. and Aung W. (1987), *Handbook of Single-Phase Heat Transfer*, John Wiley & Sons, Inc.
- Kaviany, M. (1995), *Principles of Heat Transfer in Porous Media*, Second Edition, Springer-Verlag, New York.
- Kays, W. M. and London, A. L. (1984), *Compact Heat Exchanger*, Third Edition, McGraw-Hill Company, New York.

- Kim, H. G and Nair, S. V. (1990), "Strengthening Analysis of SiC Whisker Reinforced Aluminum Alloys", *Proceedings of the 11th World Korean Scientist and Engineers Conference*, The Korean Federation of Science and Technology Societies, Seoul, Korea, Jun. 25-29, pp. 1737-1742.
- Kim, H. G. and Nair, S. V. (1991), "Modification of the Shear Lag Analysis for Strengthening Predictions in a Short Fiber or Whisker Reinforced Metal Matrix Composite," *Advanced Composite Materials*, **19**, American Ceramic Society, pp. 535-541.
- King, L. V. (1914), "On the Convection of Heat from Small Cylinders in a Stream of Fluid: Determination of the Convection Constants of Small Platinum Wires with Applications to Hot-Wire Anemometry," *Philosophical Transactions of the Royal Society of London*, **A214**, pp. 373-407
- Klett, J. W (1999a), private communication
- Klett, J W (1999b), "High Thermal Conductivity Mesophase Pitch-Derived Graphitic Foams," *Composites in Manufacturing*, **14**, 4
- Klett, J. W. and Burchell, T D (1998), "High Thermal Conductivity, Mesophase Pitch-Derived Carbon Foam," *The 43rd International SAMPE Symposium*, May 31-June 4, Anaheim, CA
- Klett, J W., Hardy, R., Romine, E., Walls, C. and Burchell, T. D. (2000a), "High-Thermal-Conductivity, Mesophase-Pitch-Derived Carbon Foams: Effect of Precursor on Structure and Properties," *Carbon*, In Press.
- Koh, J. C. Y. and Colony, R. (1974), *Journal of Heat Transfer*, **74**, pp. 324-330.

- Kroner, E (1958), "Berechnung der elasticchen Konstanten des Vielkristalls aus den konstanten des Einkristalls," *Zeitschrift fur Physik*, **151**, pp. 504-518.
- Locke, G L. (1950), "Heat Transfer and Flow Friction Characteristics of Porous Solids," *TR-No 10, Office of Naval Research Contract N6onr 251 Task 6*, Department of Mechanical Engineering, Stanford University
- London, A. L., Mitchell, J. W. and Sutherland, W. A. (1960), "Heat Transfer and Flow Friction Characteristics of Crossed-Rod Matrices," *Journal of Heat Transfer*, **82**, pp. 199-213.
- London, A. L. and Shah, R. K. (1973), "Glass-Ceramic Hexagonal and Circular Passage Surfaces - Heat Transfer and Flow Friction Design Characteristics," *Transactions of Society of Automotive Engineers*, **82**, pp 425-434.
- London, A. L , Young, M B O. and Stang, J. H. (1970), "Glass-Ceramic Surfaces, Traight Triangular Passages - Heat Transfer and Flow Friction Characteristics," *Journal of Engineering for Power*, **92**, pp. 381-389.
- Lu, T J , Stone, H. A and Ashby, M F (1998), "Heat Transfer in Open-Cell Metal Foams," *Acta Metallurgica*, **46**, 10, pp 3319-3635.
- Muki, R. and Sternberg, E , (1969), "On the Diffusion of an Axial Load from an Infinite Cylindrical Bar Embedded in an Elastics Medium," *International Journal of Solids and Structures*, **5**, pp. 587-605.
- Munson, B. R , Young, D. F. and Okishi, T. H (1994), *Fundamentals of Fluid Mechanics*, Second Edition, John Wiley & Sons, Inc

- Nair, S V and Kim, H. G. (1992), "Modification of the Shear Lag Analysis for Determination of Elastic Modulus of Short Fiber (or Whisker) Reinforced Metal Matrix Composites," *Journal of Applied Mechanics*, **59**, pp. S176-S182.
- Nardone, V C (1987), "Assessment of Models Used to Predict the Strength of Discontinuous Silicon Carbide Reinforced Aluminum Alloys," *Scripta metallurgica*, **21**, pp 1313-1318.
- Nardone, V. C. and Prewo, K. M. (1986), "On the Strength of Discontinuous Silicon Carbide Reinforced Aluminum Composites," *Scripta metallurgica*, **20**, pp 43-48.
- Nield, D. A. and Bejan, A. (1998), *Convection in Porous Media*, Second Edition, Springer-Verlag, New York.
- Oosthuizen, P. H and Naylor D (1999), Introduction to Convective Heat Transfer Analysis, WCB/McGraw-Hill.
- Paul, B (1960), "Prediction of Elastic Constants of Multiphase Materials," *Transaction of Metallurgical Society of AIME*, **218**, pp. 36-46.
- Pearce, P. and Pearce, S. (1978), *Polyhedra Primer*, Van Nostrand Reinhold Company, New York
- Richardson, T L (1987), *Composites A Design Guide*, Industrial Press Inc., pp 5-12.
- Rohsenow, W M., Hartnett, J. P. and Ganic, E. N. (1985), *Handbook of Heat Transfer Fundamental*, Second Edition, McGraw-Hill Company, New York.
- Sandu, S. S. and Hager, J. W. (1992), "Formulation of a Mathematical Process Model for the Foaming of a Mesophase Carbon Precursor," *Material Research Society Symposium Proceeding*, **270**, pp 36-40.

- Shubha, M., Shah, R. G. and Jain, A. K. (1997), "A Study of Mesophase Pitch," *Recent Trends in Carbon*, Editors O. P. Bahl, Shipra Publication, India, pp. 156-166.
- Sternberg, E. and Muki, R. (1970), "Load Absorption by a Filament in a Fiber-Reinforced Materials," *Journal of Applied Mathematics and Physics (ZAMP)*, **21**, pp. 552-569.
- Taya, M. and Arsenault, R. J. (1989), *Metal Matrix Composites: Thermo-mechanical Behavior*, Pergamon Press, pp 25-28.
- Tee, C. (2000), "Modeling of Thermal Conductivity and Pressure Drop, and Thermal Mechanical Testing of Carbon Foam-Based Materials", *Master Thesis, The University of Tennessee, Knoxville, Department of Mechanical and Aerospace Engineering and Engineering Science*.
- Thoma, H. (1921), *Hochleistungskessel*, Springer, Berlin
- Tien, C. L. and Vafai, K. (1990), "Conductive and Radiative Heat Transfer in Porous Media," *Advances in Applied Mechanics*, **27**, pp. 225-281.
- Timoshenko, S. P. and Goodier, J. N. (1951), *Theory of Elasticity*, McGraw-Hill, New York
- Tong, L. S. (1956), "Heat Transfer and Flow Friction Characteristics of Screen Matrices at High Reynolds Numbers," *TR-No.28, Office of Naval Research Contract Nonr 225(23) Task 6*, Department of Mechanical Engineering, Stanford University.
- Tong, L. S. and London, A. L. (1957), "Heat Transfer and Flow Friction Characteristics of Woven-Screen and Crossed-Rod Matrixes," *Transactions of The A S M.E.*, **79**, pp. 1558-1570.

- Tucker, C. L. and Liang, E (1999), "Stiffness Predictions for Unidirectional Short-fiber Composites: Review and Evaluation," *Composites Science and Technology*, **59**, pp. 655-671
- Vafai, K. and Tien, C. L. (1981), "Boundary and Inertia Effects on Flow and Heat Transfer in Porous Media," *International Journal of Heat and Mass Transfer*, **24**, pp 195-203.
- Zhang, Y. (1999), "Modeling of Stress Transfer in Fiber-Reinforced Ceramic Matrix Composites", *Master Thesis, The University of Tennessee, Knoxville, Department of Mechanical and Aerospace Engineering and Engineering Science*
- Žukauskas, A. (1987), "Heat Transfer from Tubes in Crossflow," *Advances in Heat Transfer*, **18**, pp. 93-160

VITA

Hairong Li was born in China on October 9, 1970. She attended the elementary school and high school and finished her undergraduate study there. From 1987 to 1991, she was well educated at Wuhan University of Hydraulic and Electric Engineering in the field of Thermal Power Engineering. After her graduation, she worked as an Assistant Engineer and then Engineer at Maanshan Power Plant and Hengxin Industry Co. Ltd. She was responsible for operation, maintenance, supervision, and design of power generation systems. She conducted mechanical and thermal testing on materials used in heater exchangers. She also designed different kinds of heater exchangers to meet the customers' requirements. In view of her excellent abilities and achievements, she was recommended to work as a Visiting Engineer in Japan in 1997 and 1999, respectively, and was responsible for international collaboration.

Starting from Fall 1999, she enrolled in the graduate program in the Department of Mechanical and Aerospace Engineering and Engineering Sciences at the University of Tennessee, Knoxville, and accepted a graduate research assistantship and a teaching assistantship. She assisted Dr. N. Yu in conducting analytical and numerical modeling on graphite foam, which exhibits a high conductivity and extremely high accessible surface areas.